CHAPTER

13

Provenance and recycling of detrital zircons from Cenozoic Altiplano strata and the crustal evolution of western South America from combined U-Pb and Lu-Hf isotopic analysis

Kurt Sundell*, Joel E. Saylor†,a, Mark Pecha*

Department of Geosciences, University of Arizona, Tucson, AZ, United States Department of Earth and Atmospheric Sciences, University of Houston, Houston, TX, United States†*

1 Introduction

Cenozoic strata in the central Andes archive valuable information about mountain-building processes that took place along the western margin of South America. In this context, the northernmost Peruvian Altiplano is a particularly excellent repository, as it contains a nearly complete record of Cenozoic sedimentation. The Altiplano is situated in the central Andean plateau (Isacks, 1988), Earth's largest modern orogenic plateau formed by ocean-continent convergent orogenesis (Allmendinger et al., 1997) (Fig. 1). Although there has been a long and rich history of geological research in the central Andes (e.g., Darwin, 1846; Forbes, 1861; Moon, 1939; Newell, 1949; Jordan et al., 1983; Isacks, 1988; Allmendinger et al., 1997; Ramos, 1999, 2009), with ample recent tectonics research in the southern central Andes of Bolivia, Argentina, and Chile (e.g., DeCelles et al., 2015a), the northern central Andes of southern Peru have only recently received renewed research focus in applied tectonics (e.g., Carlotto, 2013; Perez and Horton, 2014; Horton et al., 2015; Perez et al., 2016). Further, investigation into the crustal evolution of the western margin of South America has been focused on provinces to the east and west of the Altiplano including the Arequipa Massif (Casquet et al., 2010) and central Peruvian coast (e.g., Polliand et al., 2005) to the west; the Peruvian Eastern Cordillera (e.g., Chew et al., 2007), and Amazonian craton and peripheral regions (e.g., Santos et al., 2008) to the east; and preserved Paleozoic strata in southern Peru and northern Bolivia (e.g., Reimann et al., 2010; Bahlburg et al., 2011). Cenozoic Altiplano strata have not been interrogated in this regard.

Detailed records of orogenesis are often preserved in the isotopic compositions of detrital minerals hosted in clastic sedimentary rocks. Zircon is an ideal mineral phase for interrogating tectonic

[a]Current address: Department of Earth, Ocean and Atmospheric Sciences, University of British Columbia, Vancouver, BC, Canada.

Andean Tectonics. https://doi.org/10.1016/B978-0-12-816009-1.00014-9
© 2019 Elsevier Inc. All rights reserved.

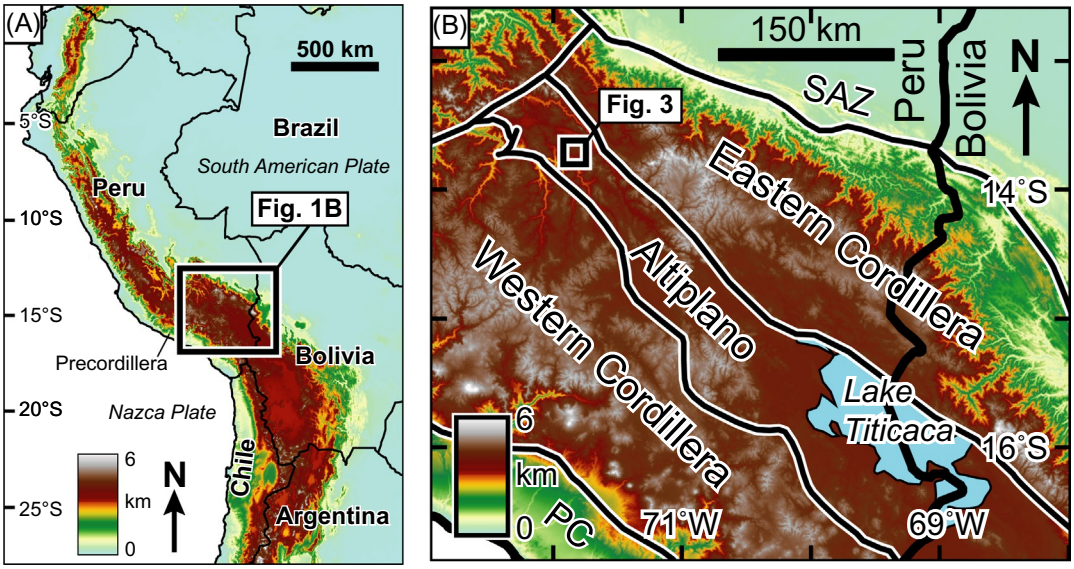

FIG. 1

(A) Digital elevation model (DEM) of the northern central Andes from HYDRO1K data. (B) DEM from Shuttle Radar Topography Mission 90 m data and physiographic regions of southern Peru. PC, Precordillera; SAZ, Subandean zone (modified from Sundell et al., 2018).

processes, as its chemical formula is simple ($ZrSiO_4$), and it incorporates high amounts of U and Hf with relatively low amounts of initial Pb (Stacey and Kramers, 1975; Belousova et al., 2010). Hf isotopic compositions in zircon are sensitive to source rock type and crystallization environment (Belousova et al., 2002), and have been used to determine the detailed geochemical evolution of continental crust (e.g., Augustsson et al., 2006; Hawkesworth et al., 2010; Belousova et al., 2010; Dhuime et al., 2011). Zircon is particularly well suited for questions addressing sediment provenance and crustal evolution through multiple orogenic cycles, as it is refractory, highly resistant to physical and chemical weathering, stable under a wide range of pressure and temperature conditions, and undergoes little post-crystallization isotopic exchange (Speer, 1980; Cherniak et al., 1997; Gehrels, 2014). Detrital zircon U-Pb geochronology is especially powerful when combined with Hf isotope geochemistry (e.g., Griffin et al., 2004), as Hf isotopic compositions provide a valuable second dimension of data for individual zircon grains (Belousova et al., 2002). These systems are complementary in understanding orogenic processes, as the former can be used to determine the crystallization histories of sediment source terranes, and the latter can be used to elucidate the crustal and magmatic evolution of a region.

We present U-Pb geochronology and Hf isotope geochemistry for detrital zircons from seven sandstone samples collected from Cenozoic Altiplano strata, interpreted in the context of two large compilations of new and published εHf(t) and εNd(t) data ($n = 2484$) and detrital zircon U-Pb ages ($n = 10{,}361$), to determine the sediment provenance and crustal evolution of western South America. Results point to a mixture of sediment sources from tectonic provinces situated both to the east and west. Following initial deposition of these zircons, this region was isolated from further sediment input resulting in recycling of detrital zircons during the development of the Andean orogen. This hypothesis is supported by U-Pb and εHf(t) patterns of detrital zircons from Paleozoic sandstones (Reimann et al., 2010;

Bahlburg et al., 2011), and comparison to a regional compilation of detrital zircon U-Pb ages, which collectively suggest that detrital zircons in Cenozoic Altiplano strata were sourced from recycled sedimentary rocks. Proterozoic crustal recycling reaches a maximum during the late Neoproterozoic, followed by a steady increase in Phanerozoic crustal generation in the late Paleozoic to Cenozoic that corresponds to the establishment of long-lived accretionary orogenesis which has continued to present day. Isotopic trends of pulsed Andean magmatism and accompanying decreases in εHf(t) provide tentative support for models of orogenic cyclicity that call on simple-shear underthrusting of continental lithosphere (DeCelles et al., 2009, 2015b).

2 Geologic context

2.1 Assembly of the South American continent

The South American continent is an amalgamation of accreted lithospheric fragments and remnant orogenic terranes (Cordani et al., 2009). Hadean to Eoarchean zircons (4.1–3.7 Ga) represent some of the oldest crustal material in South America in the São Francisco craton (Paquette et al., 2015) (Fig. 2). The northern extension of this cratonic block is the Amazonian craton, which is cored by >2.3 Ga Archean-Paleoproterozoic blocks (Cordani and Sato, 1999) (Fig. 2). Adjacent to this central core is the Paleoproterozoic to Mesoproterozoic Marconi-Icantiúnas (2.2–1.9 Ga) terrane to the northeast, and the Ventuari-Tapajos (2.0–1.8 Ga), the Río Negro-Juruena (1.8–1.55 Ga), the Rondonia-San Ignácio (1.55–1.2 Ga), and the Sunsás (Grenville equivalent) (1.2–0.9 Ga) terranes that build progressively outward to the southwest (Cordani and Sato, 1999; Santos et al., 2008; Cordani et al., 2009) (Fig. 2). The Arequipa-Antofalla terrane to the west along the Pacific coast

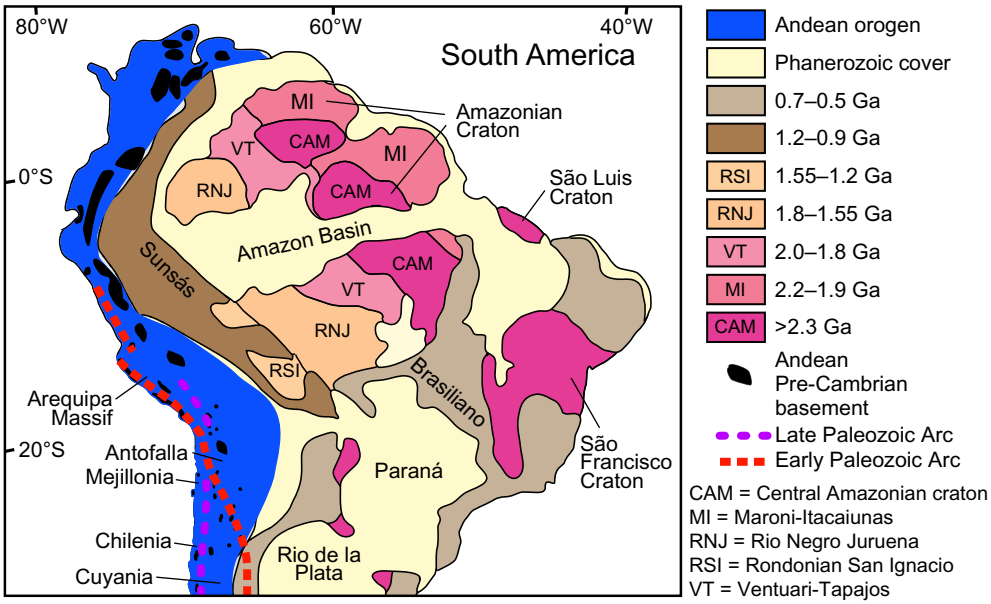

FIG. 2

Simplified age province map of South America modified from Pepper et al. (2016) and references therein.

of southern Peru and northern Chile has crystallization ages that overlap with multiple tectonic provinces in South America, as it hosts igneous and metamorphic rocks as old as 2.1–1.8 Ga, Sunsás-Grenville-related metamorphic rocks with a 1.0–0.9 Ga age range, and Ordovician-Silurian subduction-related magmatic overprinting (Loewy et al., 2004; Casquet et al., 2010).

Neoproterozoic orogenesis involved convergence between the Amazonian and São Francisco cratons, and Tocantins (central Brasiliano) province and associated crustal fragments during the amalgamation of western Gondwana (Pimentel and Fuck, 1992; Vaughan and Pankhurst, 2008). Crustal material with Neoproterozoic ages could be related to the collision and subsequent rifting of Laurentia from Gondwana and associated opening of the southern Iapetus Ocean (Rapela et al., 1998; Hartz and Torsvik, 2002). Alternatively, these ages may originate from the Neoproterozoic terranes to the east in the Brazilian shield (Pimentel and Fuck, 1992), or a hypothesized magmatic arc along a proto-Andean margin now buried beneath the modern Andean Eastern Cordillera (Chew et al., 2008). Subduction-related magmatism and deformation defines the 500–400 Ma Paleozoic Famatinian orogeny, which stretched along the western edge of South America from Patagonia to Venezuela (Aceñolaza and Toselli, 1984; Salda et al., 1992; Chew et al., 2007). Ordovician-Devonian strata in the northern Altiplano were deposited in the Peru-Bolivia trough situated between the Arequipa Massif to the west and the Amazonian craton to the east (Cobbing et al., 1977; Bahlburg et al., 2011). Late Paleozoic-Mesozoic igneous activity along the western margin of Gondwana produced abundant 350–150 Ma zircons resulting from convergence and extension due to slab rollback and subduction retreat, and the emplacement of multiple Triassic intrusive complexes in the location of the modern Peruvian Eastern Cordillera (Kontak et al., 1990).

The modern Andes are the most recent expression of orogenesis along the western margin of South America, and Earth's longest continuous modern mountain chain (Isacks, 1988; Allmendinger et al., 1997) (Fig. 1A). Ocean-continent convergence between the Nazca and South American plates has taken place along this margin since as early as the late Paleozoic (Allmendinger et al., 1997). Andean orogenesis is punctuated by periods of extensive magmatism in the early Jurassic (200–175 Ma), Late Cretaceous-early Paleocene (90–60 Ma) (Demouy et al., 2012), and throughout the Cenozoic (65 Ma–present) (Mamani et al., 2010).

The high topography that defines the modern Andean plateau can be separated into discrete physiographic regions (Fig. 1B). The Western Cordillera is the active magmatic arc. The Altiplano is the broad, flat-lying, high-elevation plateau in the longitudinally central part of the orogen. The Eastern Cordillera is the former (inactive) Cenozoic retroarc fold-and-thrust belt comprising largely deformed Paleozoic strata and Mesozoic plutons (Kontak et al., 1990; Rak et al., 2017), which formed at least in part by reactivation of preexisting Mesozoic extensional structures (Perez et al., 2016). The Subandean zone is the modern retroarc fold-and-thrust belt, and the dominant crustal load driving foreland basin flexural subsidence to the east and northeast (Fig. 1B).

2.2 Study area in the Peruvian Altiplano

The study area is located in the northernmost Altiplano of southern Peru, south of the city of Cusco (Fig. 1B). Measured stratigraphic formations are bounded by northwest-trending contractional structures that expose a nearly complete section of Cenozoic Altiplano stratigraphy (Fig. 3). Paleogene strata were deposited in a west-southwest-sourced foreland basin with flexural subsidence driven primarily by crustal loading of the emerging and encroaching Western Cordillera (Carlotto, 2013; Sundell et al., 2018) (Fig. 1). Stratigraphic formations include the Paleocene-Eocene Quilque Formation, the Eocene Kayra and Soncco formations, the Oligocene Punacancha Formation, and the late Miocene Paruro Formation (Fig. 3). These sedimentary formations formed from a mixture of fluvial and alluvial

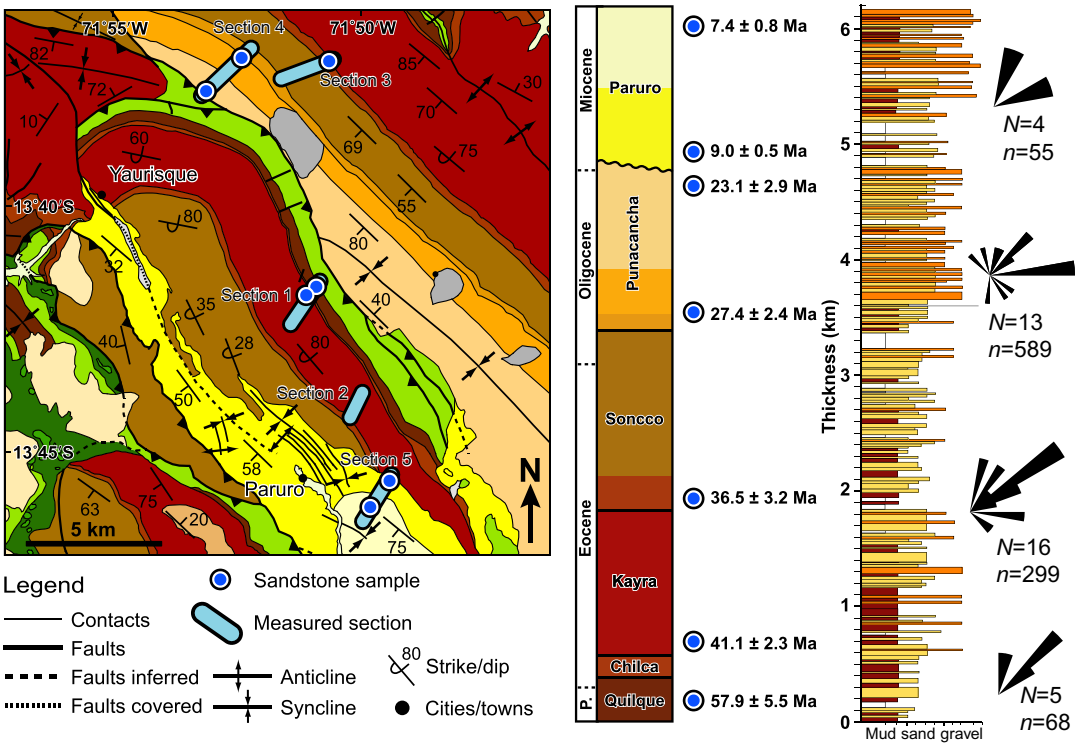

FIG. 3

Map of the study area and Cenozoic stratigraphy modified from Sundell et al. (2018). Geologic map was originally sourced from Instituto Geológico Minero y Metalúrgico (INGEMMET) and Carlotto (2013). *Triangles on fault lines* indicate thrust hanging wall. Green map units are Cretaceous sedimentary rocks. *Light blue lines* are measurement locations for the composite stratigraphic section. *Blue filled circles* are sampling locations for detrital zircon U-Pb and Hf analysis. Numbers right of Cenozoic timescale are single-grain maximum depositional ages. Paleocurrent measurements from (N = stations, n = individual measurements).

fan deposition, with an upsection increase in the latter (Fig. 3). Detailed description and measurement of strata, lithofacies characterization, sediment provenance analysis, and detrital zircon U-Pb geochronology are documented in Sundell et al. (2018).

3 Methods

Detrital zircon U-Pb geochronology and Hf isotope geochemistry was conducted at the Arizona LaserChron Center (ALC) at the University of Arizona (laserchron.org). Seven fine-grained to coarse-grained sandstone samples were collected from five Paleocene-Miocene stratigraphic formations in the northernmost Peruvian Altiplano; we use the same samples analyzed and reported in Sundell et al. (2018). Additional zircons from these sample separates were mounted in epoxy and polished. Sample mounts were imaged by backscatter electron and cathodoluminescence imaging to avoid obvious zoning and grain cracks during analysis. Individual zircon grains were measured in situ by laser ablation

inductively coupled plasma mass spectrometry (LA-ICP-MS) with a Photon Machines Analyte G2 excimer laser and small-volume HelEx cell connected to a Nu Plasma HR multicollector ICP-MS. See Gehrels and Pecha (2014) and Ibanez-Mejia et al. (2014) for ALC instrumentation details.

3.1 U-Pb geochronology

Zircons from seven sandstone samples were analyzed by LA-ICP-MS U-Pb geochronology to provide age control for Hf isotope geochemistry. Samples from the Quilque and Kayra formations (20150519-03 and 20150520-01, respectively) were ablated using a small laser spot size (10 μm and 9 s) and analyzed using discrete dynode ion counters (IC); ^{202}Hg was not measured for IC analysis. The remaining samples from the Soncco, lower and upper Punacancha, and lower and upper Paruro formations (20150525-02, 20140611-01, 20140611-03, 20140605-01, and 20140608-03, respectively) were ablated using a larger spot size and longer acquisition duration (30 μm and 15 s), and measured using 3×10^{11} ohm resistor Faraday collectors for ^{238}U, ^{232}Th, ^{208}Pb, and ^{206}Pb, and ion counters for ^{204}(Hg+Pb) and ^{202}Hg.

Isotopic ratios were corrected for elemental and mass fractionation through sample-standard bracketing using ALC's in-house data reduction scheme, AgeCalc (Gehrels et al., 2008). Sri Lanka zircon was used as the primary standard; analytical sessions were monitored using R33 as a secondary zircon standard. ^{206}Pb/^{238}U ratios were corrected for down-hole fractionation by linear regression (Košler et al., 2002). Isobaric interference between ^{204}Pb and ^{204}Hg was corrected for Faraday acquisition by measuring ^{202}Hg and subtracting ^{204}Hg based on the known natural ratio of ^{202}Hg/^{204}Hg of 4.35; no Hg correction was made for IC analysis. Results were corrected for common Pb based on regression analysis of the terrestrial Pb isotope evolution model of Stacey and Kramers (1975) and initial Pb compositions reported in their Table 6.

Best ages were assigned based on a ^{206}Pb/^{238}U to ^{206}Pb/^{207}Pb transition of 900 Ma to take advantage of increased precision and accuracy above and below this age for the ^{206}Pb/^{207}Pb and ^{206}Pb/^{238}U ratios, respectively, and to avoid splitting the ubiquitous 1300–900 Ma age population observed globally (Gehrels, 2014). Ages that met the following criteria were filtered from the final reduced data and rejected from further consideration: (i) corrected ages <900 Ma with uncertainty ≥15%; (ii) ages >900 Ma with uncertainty >10%; (iii) ages >600 Ma with discordance >20%; (iv) all analyses with reverse discordance >5%; and (v) all analyses with ^{204}Pb > 600 mean counts/s.

3.2 Hf isotope geochemistry

Hf isotope geochemistry was conducted in two separate analytical sessions following methods described in Gehrels and Pecha (2014) and Ibanez-Mejia et al. (2014). Hf has five stable isotopes, one of which, ^{176}Hf, is radiogenic, and is formed through beta decay of ^{176}Lu (Blichert-Toft, 2001). Lu-Hf-Yb isotopes were measured via LA-ICP-MS using a 40-μm laser spot for ~60 s placed over the top of the previously analyzed U-Pb laser spots. Isotopic masses (M) M180–M171 were measured using Faraday collectors to enable corrections for elemental fractionation and isobaric interference with six zircon standards: Mud Tank, 91500, Temora, Plešovice, FC1, and R33. Each isotopic measurement was baseline corrected by subtracting the mean of 40 s background measurement prior to analysis. Details of Hf fractionation corrections can be found in the Supplementary Material.

Integrations for individual samples were filtered relative to the maximum intensity for each analysis: βHf intensities >66% and >30% of the maximum for the two analytical sessions were retained to calculate mean isotopic intensities for samples in each of the two analytical sessions. The maximum and minimum intensities of the 60 1 s integrations were removed, and individual integrations were

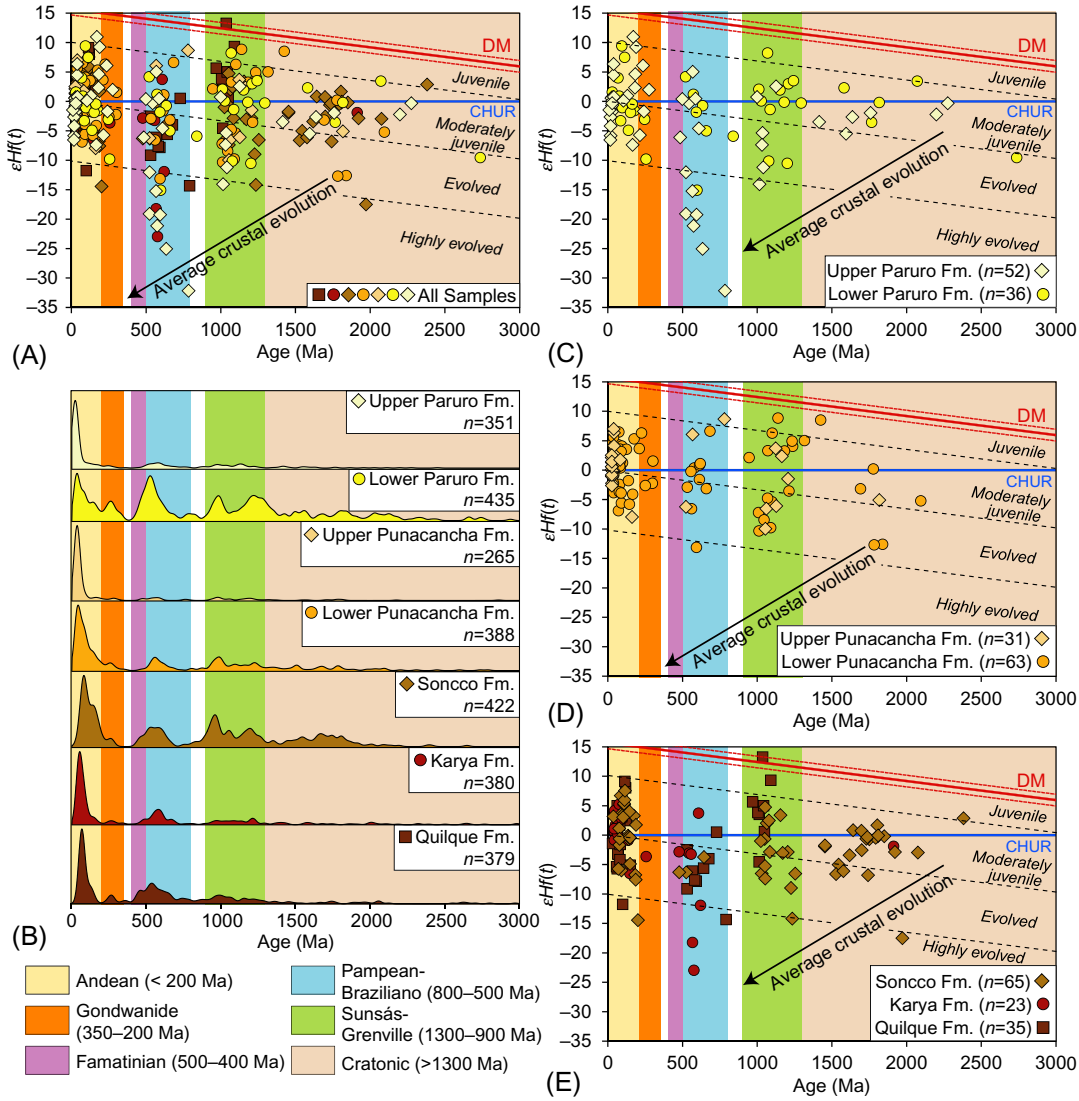

FIG. 4

Combined detrital zircon U-Pb geochronology and εHf(t) geochemical results. (A) All U-Pb–εHf(t) data from the Cenozoic Altiplano from this study ($n = 305$). (B) Kernel density estimates of U-Pb ages from this figure (20 Myr set kernel), including ages from this study and from Sundell et al. (2018), and characteristic age ranges for detrital zircon data in the northern central Andes shown as vertical bars in all plots. (C) Combined U-Pb–εHf(t) results for Miocene strata (lower and upper Paruro Formation). (D) Combined U-Pb–εHf(t) results for middle to late Oligocene strata (lower and upper Punacancha Formation). (E) Combined U-Pb–εHf(t) results for Paleocene–Eocene strata (Quilque, Kayra, and Soncco formations). DM = depleted mantle. See Section 3.2 for explanation of DM, crustal evolution line, and Chondritic uniform reservoir (CHUR).

rejected if they fell outside of 2σ (~95%) standard deviation of the remaining integrations. Finally, a test filter was applied that removes the first 10 integrations and last 10 integrations and keeps them removed if the standard uncertainty improves; this accounts for analyses that ablated through the entire grain (burn-throughs). Results are reported as the mean and 1σ standard error.

The six zircon standards analyzed during the two separate analytical sessions gave an overall offset from accepted values based on thermal ionization mass spectrometry of 0.000001 and −0.000001, and an average 1σ uncertainty of ±0.000016 and ±0.000019. A total of 87.4% and 99.8% of unknown analyses were retained after filtering the results for the first and second analytical sessions, respectively. Mean 1σ uncertainties of the unknowns are ±0.000021 and ±0.000017 for the two analytical sessions, respectively.

Hf isotope geochemical results are reported in epsilon units (ε) in reference to the chondritic uniform reservoir (CHUR) based on $^{176}Hf/^{177}Hf = 0.282785$ and $^{176}Lu/^{177}Hf = 0.0336$ (Bouvier et al., 2008). This can be expressed as: $\varepsilon Hf = [(^{176}Hf_{measured}/^{177}Hf_{measured})/(^{176}Hf_{chondrite}/^{177}Hf_{chondrite}) - 1] \times 10{,}000$, representing parts per 10,000 deviation from the chondritic evolution line (Blichert-Toft, 2001). The depleted mantle array was calculated using an initial $^{176}Hf/^{177}Hf$ value of 0.283255 and initial $^{176}Lu/^{177}Hf$ value of 0.038512 (Vervoort and Blichert-Toft, 1999). Average crustal evolution trends assume modern $^{176}Lu/^{177}Hf = 0.0093$ (Vervoort and Patchett, 1996; Vervoort et al., 1999). All εHf results are reported as εHf(t), evaluated at the timing of crystallization (t) based on U-Pb geochronology results.

3.3 Data visualization

To aid in visualization and interpretation of results, combined U-Pb–εHf(t) data are plotted as two-dimensional (2D) bivariate kernel density estimates (KDEs). Construction of bivariate KDEs follows the same basic formulation as a standard KDE (Silverman, 1986), but with generation of a 2D (x-y) grid with z-axis density values. Plotting combined U-Pb–εHf(t) data as bivariate KDEs facilitates identification of data clusters and *nonarbitrary* contouring of those clusters. To construct a bivariate KDE, each data point is converted into a Gaussian curve along the x-axis (U-Pb age) and y-axis (εHf(t) value), with a kernel bandwidth (the width of each individual Gaussian) as determined by optimization (Botev et al., 2010), or set to specified U-Pb age and epsilon unit values. Note that no new information is added except assumptions of Gaussian kernel bandwidths, which, if replaced with analytical uncertainty, would produce a bivariate probability density plot. Here, the bivariate KDEs were computed over a specified square grid of 512 × 512 cells. We used 5 Myr and 2 ε unit set kernel bandwidths for ages <200 Ma εHf(t) values, and 50 Myr and 2 ε unit set kernel bandwidths for 2000–200 Ma εHf(t) values. The bivariate KDE is a three-dimensional (3D) plot, which can be contoured based on a specified density contour interval; all contours presented here are 95% from the peak density (Fig. 5A and B). When viewed parallel to the z-axis, bivariate KDEs can be viewed as color-coded intensity plots (Fig. 5C and D).

A new standalone graphical user interface computer program, *HafniumPlotter*, was developed in MATLAB to generate bivariate KDEs. The MATLAB code, standalone applications (.app for macOS and .exe for Windows), and the forthcoming example data discussed are provided in the Supplemental Material, at kurtsundell.com/downloads, and at github.com/kurtsundell/HafniumPlotter.

3.4 Frequency analysis

In order to quantify the periodicity of previously proposed cyclic orogenic processes (e.g., DeCelles et al., 2009, 2015b), we applied frequency analysis to the <200 Ma portion of the time series of εHf(t) data. We applied the REDFIT algorithm of Schulz and Mudelsee (2002) using PAST software (Hammer et al., 2001).

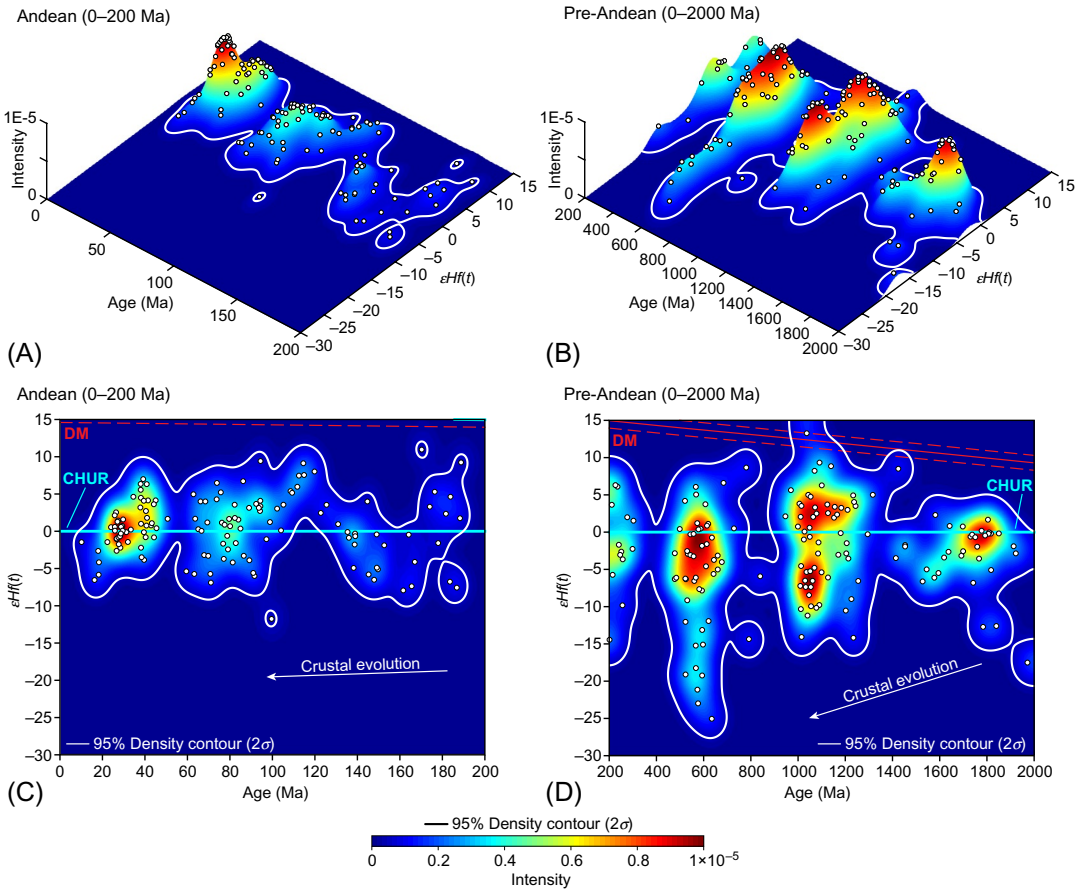

FIG. 5

Combined U-Pb–εHf(t) results plotted as bivariate kernel density estimates for (A) Andean zircons <200 Ma (5 Myr and 2ε unit set kernel bandwidths) and (B) pre-Andean zircons 2000–200 Ma (50 Myr and 2ε unit set kernel bandwidths). (C) Two-dimensional (2D) view of three-dimensional (3D) plot in part A. (D) 2D view of 3D plot in part B. DM = depleted mantle. See Section 3.2 for explanation of DM, crustal evolution line, and εHf = 0 line (Chondritic uniform reservoir, CHUR). *White lines* represent 95% of the maximum intensity in each plot.

We applied a Welch window with an oversampling rate of two, and a single segment. The data were fitted to an AR(1) red-noise model and we report the upper 95% and 99% false alarm chi-squared limits.

4 Results

4.1 U-Pb geochronology

New and previously reported detrital zircon U-Pb geochronology ages are combined and plotted as KDEs constructed using a 20-Myr kernel bandwidth (Fig. 4B). Despite the small sample sizes for new analyses (31–74 new ages per sample), all seven samples yield similar age distributions to previously

reported U-Pb data for the same samples (Sundell et al., 2018) (see Supplemental Material). A total of 388 new U-Pb ages were added to the 2231 previously reported ages (Sundell et al., 2018) for a total of 2619 detrital zircon U-Pb ages characterizing Cenozoic Altiplano strata. When new ages are combined with previous results, the age distributions are nearly indistinguishable (see Supplemental Material), indicating the detrital age distributions are well characterized.

Detrital zircon U-Pb age populations from Cenozoic strata correspond to previously documented tectonic provinces of South America (Fig. 4). Although there are upsection changes in proportions of these characteristic age populations, combined U-Pb results for all seven Altiplano samples are dominated by four groups with 14% of ages >1300 Ma, 18% between 1300 and 900 Ma, 15% between 800 and 500 Ma, and 44% <200 Ma. Ages between 500 and 400 Ma and 350–200 Ma ages are limited, totaling only 3 and 4%, respectively; the <2% of ages from 900 to 800 Ma and 400–350 Ma are not assigned to an age group.

4.2 Hf isotope geochemistry

Combined U-Pb–εHf(t) results from seven sandstone samples ($n = 305$) are considered in the age groups described earlier, summarized in Table 1, and reported in the Supplementary Material. Combined U-Pb–εHf(t) results are similar for the three main packages of Cenozoic strata (Fig. 4C–E). Paleocene-late Eocene strata (Quilque, Kayra, and Soncco formations) yield εHf(t) values of −6.5 to 1.7 for >1300 Ma zircons, −6.6 to 5.8 for 1300–900 Ma zircons, −13.7 to −0.7 for 800–500 Ma zircons, −14.4 to −3.6 for 350–200 Ma zircons, and −3.8 to 4.9 for <200 Ma zircons. Oligocene strata (lower and upper Punacancha Formation) yield εHf(t) values of −10.2 to 4.0 for >1300 Ma zircons, −7.7 to 4.2 for 1300–900 Ma zircons, −6.5 to 4.9 for 800–500 Ma zircons, −2.3 to 4.9 for 350–200 Ma zircons, and −3.1 to 4.0 for zircons <200 Ma. Late Miocene strata (lower and upper Paruro Formation) yield εHf(t) values of −5.6 to 1.3 for >1300 Ma zircons, −8.4 to 3.9 for 1300–900 Ma zircons, −20.4 to 1.5 for 800–500 Ma zircons, −7.2 to 3.1 for 350–200 Ma zircons, and −3.8 to 5.0 for zircons <200 Ma. The 1σ ranges of εHf(t) values of combined Cenozoic samples of the five dominant age populations yield −7.2 to 2.2 for >1300 Ma zircons, −7.5 to 4.8 for 1300–900 Ma zircons, −15.2 to 2.7 for 800–500 Ma zircons, −7.6 to 3.9 for 350–200 Ma zircons, and −3.6 to 4.6 for zircons <200 Ma (Fig. 4 and Table 1).

In general, positive εHf(t) values are representative of more juvenile, primitive mantle reservoir material (bulk silicate Earth, εHf = 0), whereas more negative εHf(t) values are indicative of derivation from older crustal material with an earlier timing of mantle extraction (Belousova et al., 2002). However, εHf(t) results above or below CHUR (εHf = 0) do not necessarily correspond to juvenile or evolved crust because the difference in $^{176}Hf/^{177}Hf$ between the depleted mantle and continental crust increases with time (Belousova et al., 2002). Therefore, to describe the relative evolution patterns of combined U-Pb–εHf(t) results, we adopt a modified convention of Reimann et al. (2010) and Bahlburg et al. (2011), which is based on the number of ε unit deviation from the depleted mantle array. Note that εHf(t) values cannot in theory be more positive than the depleted mantle array, so deviation is in the negative direction. We consider results within 5 ε units of the depleted mantle to be "juvenile," results between 5 and 15 ε units deviation to be "moderately juvenile," results between 15 and 25 ε units deviation to be "evolved," and deviations >25 ε units below the depleted mantle array to be "highly evolved." To indirectly compare our results to published εNd(t) values (e.g., DePaolo, 1988), we consider published εNd(t) values 5 ε units or less below the depleted mantle array as "juvenile," 5–10 ε units below to be "moderately juvenile," 10–15 ε units to be "evolved," and 15 or more ε units to be "highly evolved." See Table 2 and Supplementary Material for complete data compilations and additional comparison plots.

Table 1 Detrital zircon U-Pb and εHf results (1σ range)

			Cratonic (>1300 Ma)			Sunsás-Grenville (1300–900 Ma)			Pampean-Braziliano (800–500 Ma)			Famatinian (500–400 Ma)			Gondwanide (350–200 Ma)			Andean (<200 Ma)		
	Region	**Stratigraphic age**	*n*	**Min εHf(t)**	**Max εHf(t)**	*n*	**Min εHf(t)**	**Max εHf(t)**	*n*	**Min εHf(t)**	**Max εHf(t)**	*n*	**Min εHf(t)**	**Max εHf(t)**	*n*	**Min εHf(t)**	**Max εHf(t)**	*n*	**Min εHf(t)**	**Max εHf(t)**
Upper Paruro Fm.	Altiplano	Late Miocene	6	−4.3	−1.1	6	−11.7	0.2	11	−24.3	−1.8	2	−6.1	0.4	4	−4.2	4.6	23	−4.0	4.8
Lower Paruro Fm.	Altiplano	Late Miocene	5	−6.2	3.2	11	−5.7	5.0	7	−9.1	2.5	N/A	N/A	N/A	2	−9.8	−3.1	11	−3.3	5.2
Upper Punacancha Fm.	Altiplano	Late Oligocene	1	−5.1	−5.1	6	−7.9	1.9	3	−3.7	9.3	N/A	N/A	N/A	N/A	N/A	N/A	21	−2.3	3.9
Lower Punacancha Fm.	Altiplano	Oligocene	7	−10.4	4.7	14	−7.5	5.1	10	−6.8	3.1	N/A	N/A	N/A	5	−2.1	4.8	27	−3.7	4.1
Soncco Fm.	Altiplano	Late Eocene	22	−6.6	1.7	15	−8.1	1.9	2	−6.3	−3.7	1	−6.3	−6.3	1	−14.4	−14.4	24	−3.5	5.2
Kayra Fm.	Altiplano	Eocene	1	−1.9	−1.9	N/A	N/A	N/A	6	−18.6	0.0	1	−2.8	−2.8	1	−3.6	−3.6	14	−1.7	3.7
Quilque Fm.	Altiplano	Late Paleocene	N/A	N/A	N/A	8	−0.4	9.6	9	−10.3	−2.3	N/A	N/A	N/A	N/A	N/A	N/A	18	−5.5	4.9
Paruro Fm. (All)	Altiplano	Late Miocene	11	−5.6	1.3	17	−8.4	3.9	17	−20.4	1.5	2	−6.1	0.4	6	−7.2	3.1	34	−3.8	5.0
Punacancha Fm. (All)	Altiplano	Oligocene	8	−10.2	4.0	20	−7.7	4.2	13	−6.5	4.9	N/A	N/A	N/A	5	−2.3	4.9	48	−3.1	4.0
Quilque/ Kayra/ Soncco Fms.	Altiplano	Paleocene-Eocene	23	−6.5	1.7	23	−6.6	5.8	17	−13.7	−0.7	2	−6.3	−2.8	2	−14.4	−3.6	56	−3.8	4.9
All Cenozoic Altiplano	Altiplano	Cenozoic	42	−7.2	2.2	60	−7.5	4.8	47	−15.2	2.7	4	−6.5	−1.0	13	−7.6	3.9	138	−3.6	4.6

Table 2 Compilation of εHf and εNd data ranges

	Analysis type	>1300 Ma		1300–900 Ma		800–500 Ma		500–400 Ma		350–200 Ma		<200 Ma	
		Min ε	Max ε	Min ε	Max ε	Min ε	Max ε	Min ε	Max ε	Min ε	Max ε	Min ε	Max ε
Detrital εHf													
This Study S Peru Altiplano	εHf	−17.5	8.5	−14.2	13.3	−32.2	8.7	−6.3	0.4	−14.4	6.3	−11.8	11.0
Augustsson et al. (2006) W Argentina	εHf	−2.0	7.3	−7.4	12.0	−28.8	0.6	−2.5	−1.1	2.0	2.0	–	–
Bahlburg et al. (2009) N Chile	εHf	−18.5	11.2	−8.1	11.5	−11.8	8.1	−11.1	4.1	−14.5	3.4	–	–
Bahlburg et al. (2011) S Peru Eastern Cordillera	εHf	−8.4	−2.9	−4.9	−3.5	0.8	1.3	−9.4	−6.3	–	–	–	–
Boekhout et al. (2015) S Peru Coastal Cordillera	εHf	–	–	–	–	–	–	−7.0	−4.4	−40.1	7.0	−30.2	6.8
Otamendi et al. (2017) NW Argentina	εHf	−7.7	2.8	−1.8	1.6	−6.5	−2.1	–	–	–	–	–	–
Pepper et al. (2016) C Andes Modern Rivers and Beaches	εHf	−18.7	13.6	−21.0	20.6	−31.8	12.2	−13.4	4.2	−14.9	5.0	−15.9	13.9
Reimann et al. (2010) S Peru Altiplano	εHf	−6.6	1.7	−12.6	5.2	–	–	–	–	–	–	–	–
Reimann et al. (2010) S Peru Coastal Cordillera	εHf	−24.2	8.9	−19.6	12.0	−13.6	5.9	−32.8	0.7	−9.5	0.2	–	–
Reimann et al. (2010) S Peru and N Bolivia Eastern Cordillera	εHf	−17.3	6.7	−17.8	9.2	−13.1	11.3	−15.1	−11.8	–	–	–	–
Willner et al. (2008) C Chile	εHf	−20.0	9.4	−6.4	13.0	−7.7	9.9	−10.6	9.2	−3.2	4.1	–	–
In situ εHf													
Boekhout et al. (2015) S Peru Coastal Cordillera	εHf	–	–	–	–	–	–	–	–	–	–	−3.7	7.2
Chew et al. (2007) N & C Peru	εHf	–	–	–	–	–	–	−8.8	2.0	−4.3	0.5	–	–
Dahlquist et al. (2013) NW Argentina	εHf	–	–	–	–	–	–	−18.9	−1.5	−8.0	1.6	–	–
De Haller et al. (2006) C Peru Coast	εHf	–	–	–	–	–	–	–	–	–	–	5.1	7.7

Demouy et al. (2012) SW Peru	εHf	–	–	–	–	–	–	–	–	–	–	−9.5	3.3
Mišković and Schaltegger (2009) Peru Eastern Cordillera	εHf	7.1	7.1	−4.9	2.9	−5.2	0.7	−5.5	−5.5	−2.7	0.0	−2.8	4.7
Montecinos et al. (2008) C Chile	εHf	–	–	–	–	–	–	–	–	–	–	6.9	9.6
Otamendi et al. (2017) NW Argentina	εHf	–	–	–	–	−0.9	−0.9	−8.7	0.5	–	–	–	–
Polliand et al. (2005) C Peru Western Flank	εHf	–	–	–	–	–	–	–	–	–	–	5.5	11.0
Spikings et al. (2016) S Peru Eastern Cordillera	εHf	–	–	–	–	–	–	–	–	−4.5	4.1	–	–
In situ εNd													
Babinski et al. (1996) SE Brazil	εNd	–	–	–	–	−28.0	6.6	–	–	–	–	–	–
Cardona et al. (2009) C Peru Eastern Cordillera	εNd	–	–	–	–	–	–	−12.5	−6.3	−13.1	−7.1	–	–
Dahlquist et al. (2013) NW Argentina	εNd	–	–	–	–	–	–	−5.9	−2.9	–	–	–	–
de Assis Janasi (2002) SE Brazil	εNd	–	–	–	–	−14.5	−2.9	–	–	–	–	–	–
Loewy et al. (2004) SW Peru & N Chile Arequipa-Antofalla (northern)	εNd	−4.3	2.9	–	–	–	–	−9.4	−3.3	–	–	–	–
Loewy et al. (2004) SW Peru & N Chile Arequipa-Antofalla (central)	εNd	−4.6	0.2	−2.9	3.9	−6.3	6.6	−11.6	−4.6	–	–	–	–
Loewy et al. (2004) SW Peru & N Chile Arequipa-Antofalla (southern)	εNd	–	–	–	–	–	–	–	–	−2.2	−2.2	–	–
Martins et al. (2004) SE Brazil	εNd	−5.8	−4.1	–	–	−23.8	−4.1	–	–	–	–	–	–
Miller and Harris (1989) N Bolivia Eastern Cordillera	εNd	–	–	–	–	–	–	–	–	−6.2	−0.5	−10.6	−4.7

Continued

Table 2 Compilation of εHf and εNd data ranges—cont'd

	Analysis type	>1300 Ma		1300–900 Ma		800–500 Ma		500–400 Ma		350–200 Ma		<200 Ma	
		Min ε	Max ε	Min ε	Max ε	Min ε	Max ε	Min ε	Max ε	Min ε	Max ε	Min ε	Max ε
Pankhurst et al. (1998) NW Argentina	εNd	–	–	–	–	–	–	−7.3	−4.2	–	–	–	–
Pimentel and Fuck (1992) C Brazil	εNd	–	–	2.5	6.9	0.2	6.5	–	–	–	–	–	–
Rapela et al. (1998) NW Argentina	εNd	–	–	–	–	−7.7	−3.0	−4.8	1.5	–	–	–	–
Rapela et al. (2003) SE Argentina	εNd	–	–	–	–	−9.2	1.0	–	–	–	–	–	–
Santos et al. (2008) E Bolivia	εNd	−4.0	4.1	−0.2	−0.2	–	–	–	–	–	–	−2.4	−2.4
Sato et al. (2003) E Brazil	εNd	−9.2	0.8	–	–	−23.0	1.6	–	–	–	–	–	–
Spikings et al. (2016) S Peru Eastern Cordillera	εNd	–	–	–	–	–	–	–	–	−4.2	6.2	–	–

Bivariate KDEs facilitate the comparison of Cenozoic Altiplano U-Pb–εHf(t) results to other crustal provinces in South America (Figs. 5–8). These patterns may be directly compared to detrital and in situ records of εHf(t) in order to determine the provenance of detrital zircons. Results plotted as bivariate KDEs are separated into two groups, <200 Ma (Fig. 6) and 200–2000 Ma (Fig. 7), in order to highlight trends and clusters of U-Pb–εHf(t) results, and because the large relative proportion of detrital zircons <200 Ma tends to dominate the bivariate KDE intensity plots. Detrital zircons with

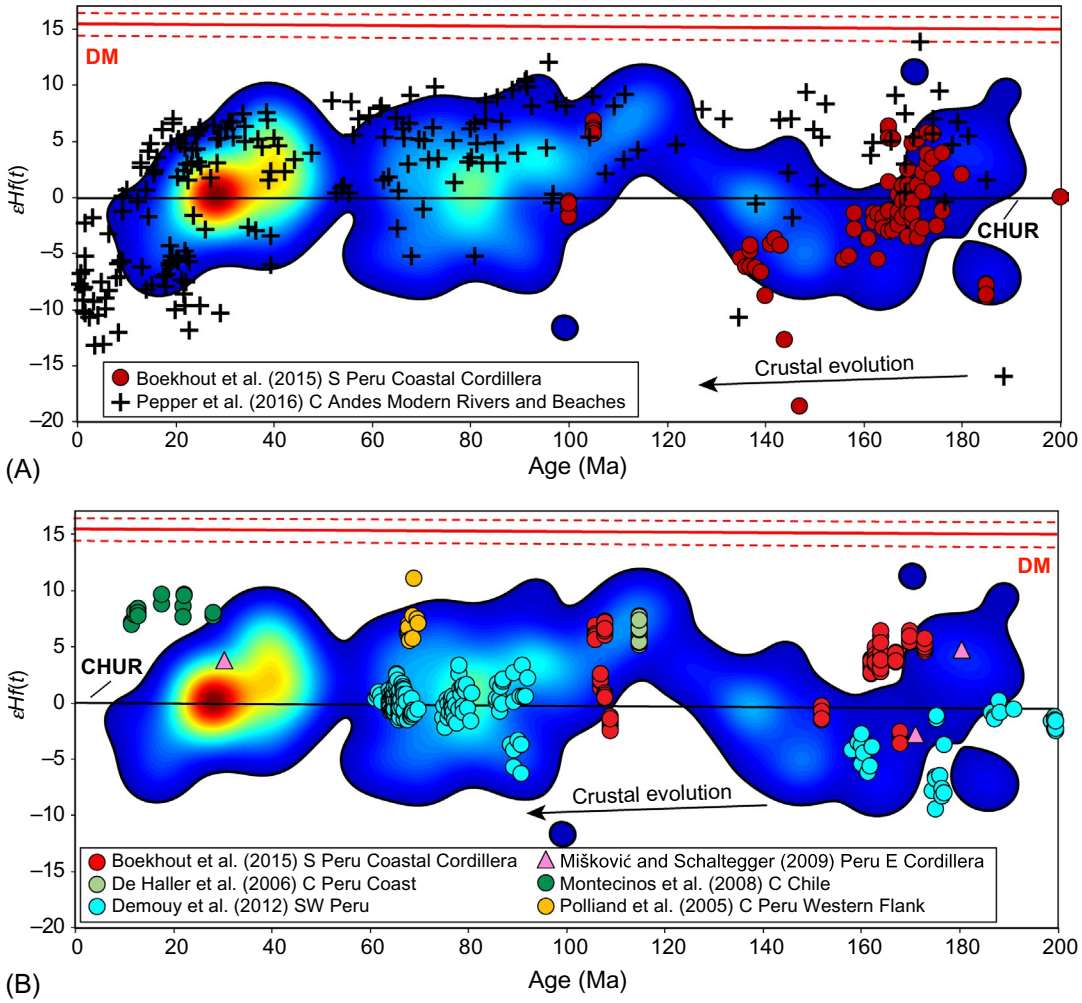

FIG. 6

Previously published detrital (A) and in situ (B) εHf(t) data plotted over contoured bivariate kernel density estimate of U-Pb–εHf(t) for detrital zircons <200 Ma from Fig. 5C. DM = depleted mantle. See Section 3.2 for explanation of DM, crustal evolution line, and εHf = 0 line (Chondritic uniform reservoir, CHUR).

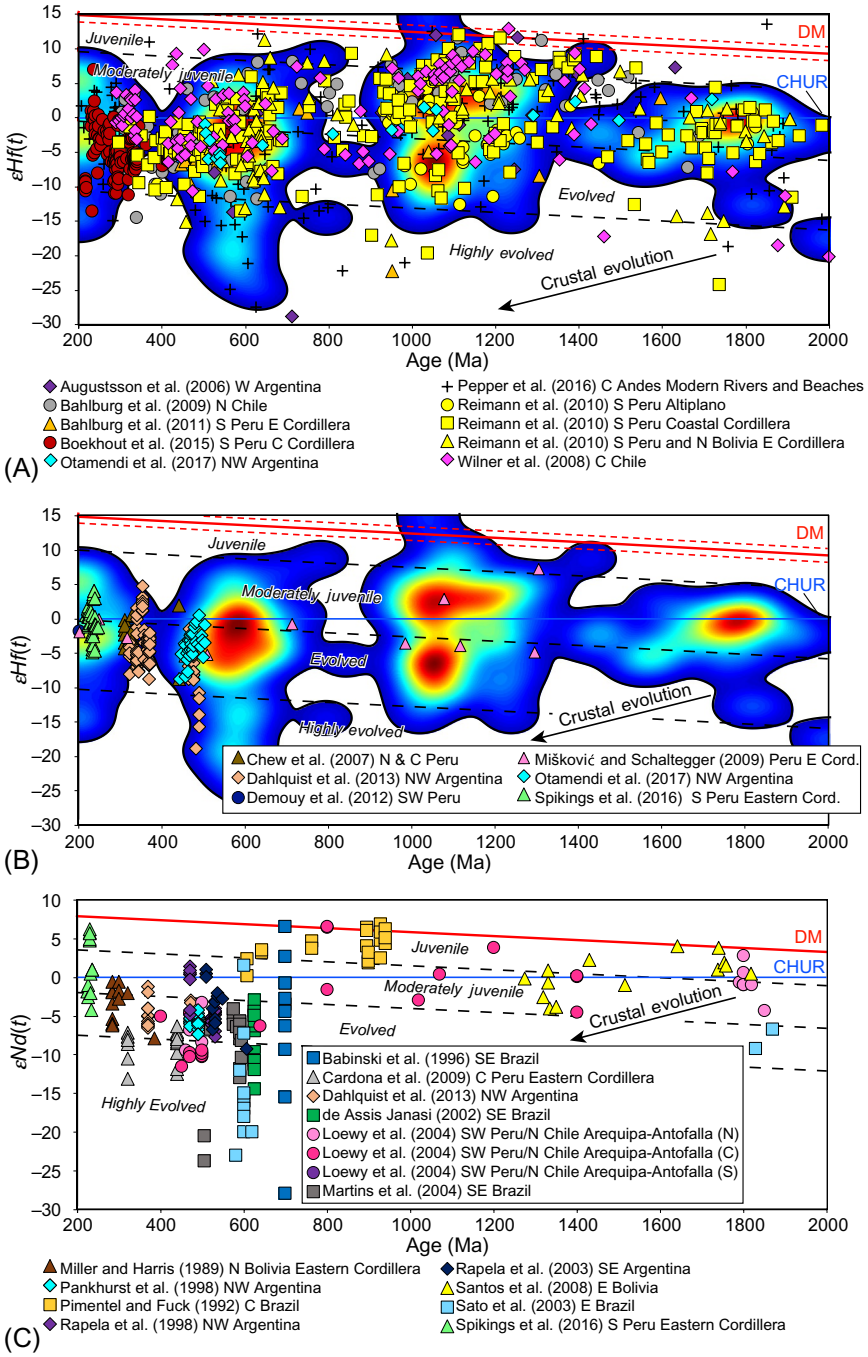

FIG. 7

Previously published (A) detrital εHf(t) data and (B) in situ εHf(t) data plotted over contoured bivariate kernel density estimates of U-Pb–εHf(t) for 2000–200 Ma from Fig. 5D. (C) Published in situ εNd(t) data from crustal provinces in South America. DM = depleted mantle. See Section 3.2 for explanation of DM, crustal evolution line, and εHf = 0 line (Chondritic uniform reservoir, CHUR).

<200 Ma crystallization ages show εHf(t) isotopic pull-downs (dispersion arrays toward more negative εHf(t) values) at 180–140 Ma, 120–60 Ma, and 50–10 Ma (Fig. 5A and C). Detrital zircons with 2000–200 Ma crystallization ages show longer-term εHf(t) isotopic pull-downs from 1800 to 1500 Ma and 1000–500 Ma (Fig. 5B and D).

Frequency analysis of the <200 Ma portion of the time series of εHf(t) data yields only one significant peak with a period of 72 Myr (Fig. 10). This is the only peak rises above the 95% false alarm limit with a period >10 Myr.

5 Discussion

5.1 Detrital zircon provenance

Combining εHf(t) geochemical data with traditional U-Pb detrital zircon geochronology provides a valuable second dimension of information for interpretations of sediment provenance. Despite upsection differences in proportions of age populations in U-Pb age distributions from Cenozoic Altiplano strata (Fig. 4B), U-Pb–εHf(t) patterns for the five stratigraphic intervals show many similarities (Fig. 4C–E). This suggests that although there were Cenozoic changes in sediment provenance from recycling of Mesozoic and subordinate Paleozoic formations based on detrital zircon U-Pb mixture modeling (Sundell et al., 2018), the detrital zircons from these recycled formations share a common underlying source. In the following, we consider a single merged data set of U-Pb–εHf(t) results for the Cenozoic Altiplano data. We use bivariate KDEs of this merged data set to facilitate interpretations of initial derivation of detrital zircons from crustal provinces across South America (Fig. 5, Section 4.2).

Comparison data for >1300 Ma crustal provinces are too limited to conclusively infer derivation of detrital zircons in Cenozoic Altiplano strata. However, there are sufficient data to speculate on the nearby and highly distal crustal provinces through indirect comparison to published εNd(t) data. Detrital zircons >1300 Ma show moderately juvenile to highly evolved εHf(t) values that vary with age (Figs. 4A and 7B). These results are inconsistent with derivation from juvenile to moderately juvenile Precambrian basement rocks of the northern Arequipa Massif to the southwest (Loewy et al., 2004) and distal crustal provinces in eastern Bolivia (Santos et al., 2008) (Fig. 7B and C). Results are consistent with the evolved εNd(t) values for 1900–1800 Ma crust of the southern South American platform Atuba complex in eastern Brazil (Sato et al., 2003) (Fig. 7C). Evolved >2500 Ma Pan-African granitoids from southeast Brazil (Martins et al., 2004) are consistent with our single data point at ~2700 Ma (εHf(t) = −9.5) (see Supplemental Material). This interpretation is tenuous because εHf(t) data are absent and εNd(t) data are limited for the overwhelming spatial coverage of the South American interior from which >1300 Ma zircons may have been derived.

The εHf(t) results from 1300 to 900 Ma detrital zircons show a wide range from juvenile to highly evolved (Fig. 7B and C, Table 2). These results are consistent with derivation from central Andean sources such as the moderately juvenile basement rocks of the central Arequipa-Antofalla province to the southwest (Loewy et al., 2004) and the Peruvian Eastern Cordillera to the east (Mišković and Schaltegger, 2009). Results are also consistent with moderately juvenile to evolved granitoid and gneissic rocks from the distal Sunsás province to the east (Santos et al., 2008). Results are inconsistent

with juvenile 950–900 Ma southern Tocantins province in the central Brasília belt (Pimentel and Fuck, 1992) (Fig. 2). This interpretation is consistent with that of Reimann et al. (2010), who cautiously suggested that detrital zircons from Paleozoic sandstones in the Eastern Cordillera of southern Peru and northern Bolivia may have originated from the Arequipa Massif to the southwest, and that detrital zircons in Paleozoic strata of the Peruvian Altiplano and Coastal Cordillera were sourced from a mixture of detritus from the east in the Sunsás province, the Amazonian craton, and Brazilian shield. However, evolved to highly evolved εHf(t) values are only seen in the detrital data (Fig. 7A) and not in any of the in situ εHf(t) and εNd(t) data (Fig. 7B and C); the evolved in situ data from the Peru Eastern Cordillera (Mišković and Schaltegger, 2009) do not appear to be related to the major isotopic pull down in this age range. It remains an open question where these detrital zircons were initially sourced, as there are currently no candidate in situ sources for the major pull down. Potential regions containing this undocumented, highly evolved crust of 1300–900 Ma in South America include the Arequipa-Antofalla province to the southwest and the Sunsás province to the east. Regardless of where these zircons initially came from, they must have already been in the central Andes by the Early Paleozoic, as they make up a significant portion of the εHf(t) detrital zircon data from Ordovician-Devonian sandstones (Reimann et al., 2010).

Detrital zircons in the 800–500 Ma age range yield εHf(t) values with more dispersion and the strongest isotopic pull down to highly evolved εHf(t) values compared to any other age group (Figs. 4A and 5D). Results are consistent with initial derivation of detrital zircons from central Andean sources such as the moderately juvenile magmatic rocks in the Peruvian Eastern Cordillera (Mišković and Schaltegger, 2009), the northern and central segments of the Arequipa-Antofalla massif (Loewy et al., 2004), and the pre-Andean margin of Gondwana in the Argentine Sierras Pampeanas (Rapela et al., 1998) (Fig. 7). However, none of these sources can account for the major isotopic pull down observed in our new detrital data. The only potential sources for the highly evolved late Neoproterozoic to early Paleozoic detrital zircons are the crustal provinces in eastern and southeastern Brazil (e.g., de Assis Janasi, 2002; Martins et al., 2004; Sato et al., 2003; Babinski et al., 1996). The juvenile-to-moderately juvenile εNd(t) values reported for southeast Brazil (Babinski et al., 1996) and syncollisional peraluminous granites in central Brazil formed during the closure of a large oceanic basin to the west of the São Francisco Craton (Pimentel and Fuck, 1992; Fuck et al., 1993) are also consistent with results from Cenozoic Altiplano detrital zircons. Derivation of zircons from these highly distal sources in central and southeastern Brazil suggests there may have been transcontinental drainage across the South American continent that was roughly the scale of the modern Amazon drainage basin, similar to that proposed for Paleozoic Laurentia (Gehrels et al., 2011). Because the major late Neoproterozoic isotopic pull down to highly evolved εHf(t) values is seen in detrital zircons in Cenozoic Altiplano strata and modern sediments (Pepper et al., 2016), but not in Ordovician-Devonian strata (Reimann et al., 2010), we infer that such a transcontinental drainage system could have only tapped central and southeastern Brazil in the late Paleozoic to Mesozoic, subsequent to deposition of Ordovician-Devonian sandstones in the central Andes. This is supported by paleogeographic reconstructions placing South America near the south pole in the early Paleozoic (e.g., Hartz and Torsvik, 2002), where it would be in a polar desert. By the late Paleozoic, South America was lower latitudes and Earth was transitioning from icehouse to hothouse conditions where it remained until the middle Jurassic (Scotese, 2004), which would have provided ample headwaters to drive such a large transcontinental drainage system.

Detrital zircons from Cenozoic Altiplano strata with 350–200 Ma crystallization ages point to westward drainage and dominant sourcing from the proximal Eastern Cordillera of southern Peru and northern Bolivia. The εHf(t) results are most similar to moderately juvenile to evolved Paleozoic and Mesozoic igneous rocks of the Eastern Cordillera in southern Peru (Chew et al., 2007; Mišković and Schaltegger, 2009; Spikings et al., 2016), which show complete overlap with the Cenozoic Altiplano U-Pb–εHf(t) bivariate KDE (Fig. 7B). Published εNd(t) records also support an Eastern Cordilleran source from southern Peru (Mišković and Schaltegger, 2009; Spikings et al., 2016) and northern Bolivia (Miller and Harris, 1989). Although εHf(t) values from central and northern Peru (Chew et al., 2007) are consistent with results from Cenozoic Altiplano sandstones, εNd(t) data reported by Cardona et al. (2009) show a stronger isotopic pulldown to highly evolved values that rules it out as a potential source (Fig. 7C). Similarly, northwest Argentina shows too strong an isotopic pull down to be considered a significant source of 350–200 Ma detrital zircons (Dahlquist et al., 2013) (Fig. 7C).

Detrital zircons younger than 200 Ma are the most prominent age group represented in Cenozoic Altiplano strata, and are most closely matched to sources along the southwestern Peruvian margin (Fig. 6B). Proximal sources likely shared the same magmatism in southern Peru, and thus are expected to have similar εHf(t) values for zircons formed from that magmatism. Specifically, detrital zircon εHf(t) values are similar to those of the Coastal Cordillera (Boekhout et al., 2015) the Coastal Batholith near Arequipa (Demouy et al., 2012), and the central coast of Peru (Polliand et al., 2005; De Haller et al., 2006). Results are also consistent with limited data from the Peruvian Eastern Cordillera (Mišković and Schaltegger, 2009). Unlikely sources include the juvenile volcanic and plutonic rocks of central Chile (Montecinos et al., 2008) and from the northern Bolivian Eastern Cordillera based on granite and pelite samples with highly evolved εNd(t) values (Miller and Harris, 1989) (Table 2). Although detrital zircons with 200–60 Ma crystallization ages may have been sourced from a combination of eastern and western sources, independent geologic observations and mixture modeling of detrital zircon U-Pb age distributions suggest that Altiplano sedimentary rocks were consistently sourced from recycled Mesozoic and subordinate Paleozoic siliciclastic rocks in the Western Cordillera throughout the Cenozoic (Sundell et al., 2018).

5.2 Detrital zircon recycling

Although Cenozoic Altiplano detrital zircons were initially derived from a mixture of crustal provinces across South America, they were ultimately sourced from recycled Paleozoic and Mesozoic sedimentary rocks in the Peruvian Western Cordillera (Sundell et al., 2018). This suggests that pre-Andean detrital zircons were first delivered to the central Andean region, then subsequently reworked, recycled, and combined with younger magmatic zircons formed during Mesozoic-Cenozoic magmatism. The likely sources for Gondwanide and younger detrital zircons (<350 Ma) are limited to regions proximal to the modern Altiplano in southern Peru. This suggests that the central Andes of southern Peru were isolated from direct input from distal age provinces at some point between the late Paleozoic and Cenozoic, and that pre-Gondwanide detrital zircons have been continuously recycled since their introduction to the western margin of South America.

We test this hypothesis by comparing detrital U-Pb and εHf(t) patterns from the Cenozoic Altiplano to records from early Paleozoic sedimentary rocks and modern rivers. If the region was indeed isolated from older, distal sediment input during Andean orogenesis, then detrital zircon U-Pb–εHf(t) patterns

should be similar since that time, as they are predicted to come from the same underlying population of detrital zircon grains. The εHf(t) values of zircons >200 Ma from Cenozoic Altiplano sandstones and modern rivers draining the eastern and western flanks of the central Andes (Pepper et al., 2016) show similar results to detrital zircons from Ordovician-Devonian sandstones (Bahlburg et al., 2011; Reimann et al., 2010) (Fig. 8). Bivariate KDE 95% density contours of εHf(t) values for 2000–200 Ma detrital zircons from modern rivers (Pepper et al., 2016) and Paleozoic sandstones (Reimann et al., 2010) show >70% overlap with that of the Altiplano εHf(t) data (Fig. 8). However, bivariate KDE contours highlight a major difference between Cenozoic and Paleozoic U-Pb–εHf(t) patterns: Paleozoic sandstones lack the highly evolved population of Neoproterozoic detrital zircons (Fig. 8). This suggests that although there was a new source of Late Neoproterozoic grains during the Late Paleozoic—Mesozoic, perhaps delivered via transcontinental drainage (see previous section), that the majority of detrital zircons have been continuously recycled since their introduction to the western margin of South America in the Paleozoic.

A second test of the hypothesis that pre-Andean detrital zircons were sourced from reworked and recycled sedimentary rocks is based on a compilation of available detrital zircon U-Pb data from across the northern central Andes of southern Peru and northern Bolivia. In total, 35 samples were combined based on geologic formation and age from $N = 99$ individual samples and $n = 10{,}361$ individual ages (Fig. 9A and B, see Table 3 for complete reference list and metadata). Although there is considerable scatter among the individual age distributions from the 35 samples, the same characteristic age groups discussed here are prominent, regardless of geographic location (Fig. 9C). Further, the compiled

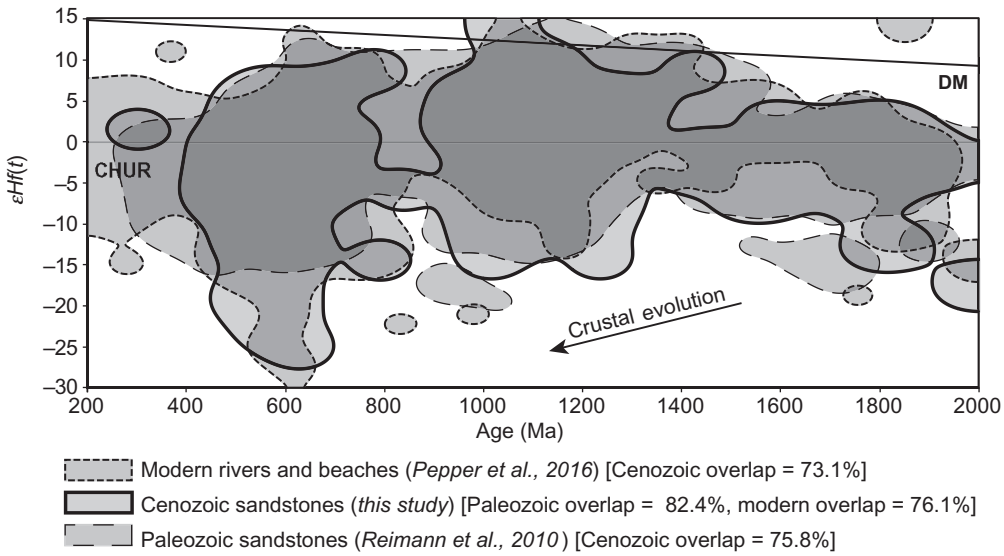

FIG. 8

Comparison of Cenozoic Altiplano U-Pb–εHf(t) 95% density contours for 2000–200 Ma detrital zircons from central Andean modern rivers and beaches (Pepper et al., 2016), Cenozoic Altiplano sandstones (this study), and Paleozoic sandstones (Reimann et al., 2010). Note that the Paleozoic contour does not share the significant late Neoproterozoic isotopic pull down of the Cenozoic and modern U-Pb–εHf(t) contours.

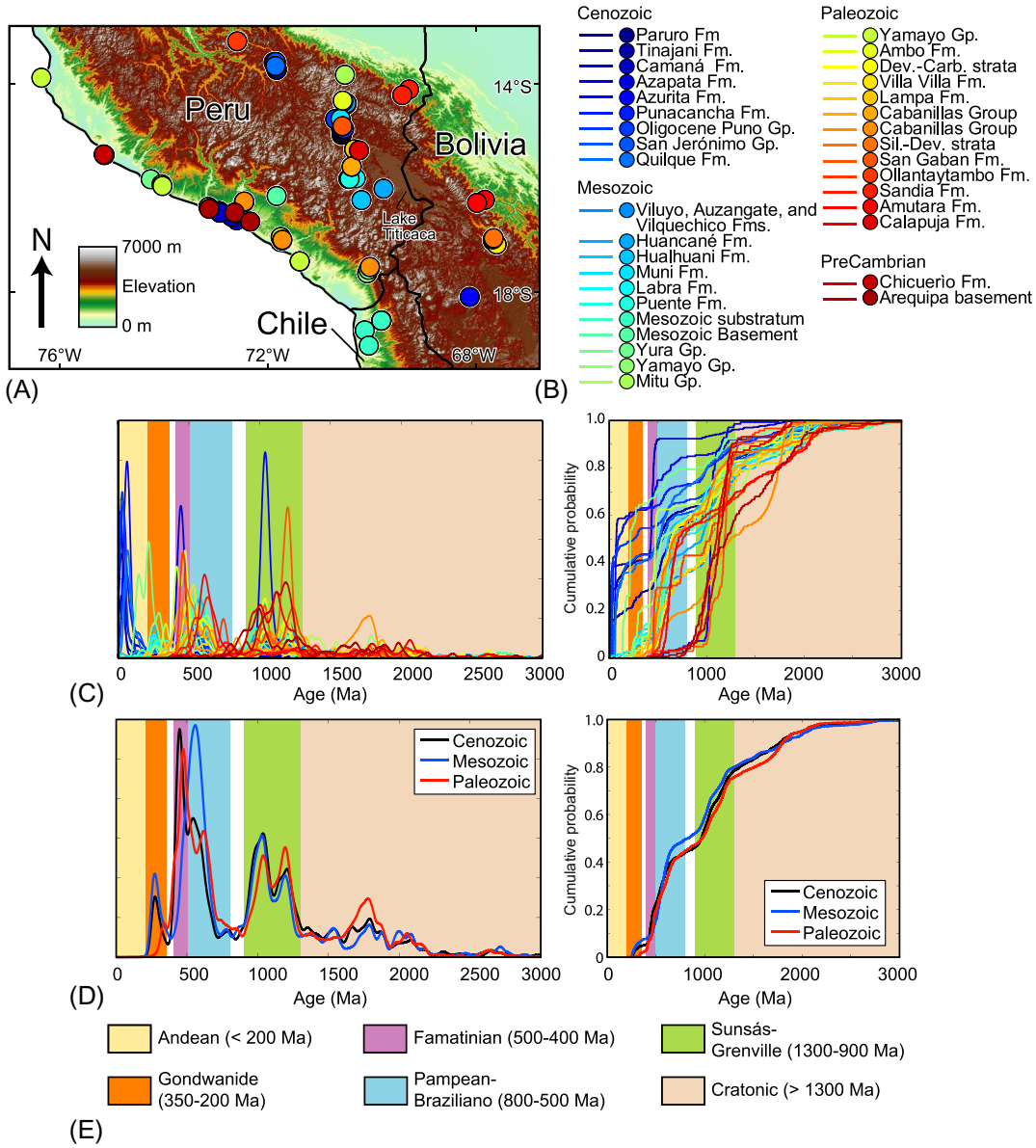

FIG. 9

Compilation of detrital zircon U-Pb data from across the northern central Andes. (A) Map of sample locations listed in Table 1. (B) Legend for samples combined based on geologic formation and depositional age from N = 99 individual samples and n = 10,361 individual ages combined into 35 sample distributions (see Table 3 for complete reference list and metadata). (C) Age distributions plotted as kernel density estimates (KDEs) (left) and cumulative distribution functions (CDFs) for samples listed in parts A and B. (D) Samples combined by Phanerozoic Era with Andean ages removed. (E) Characteristic age ranges for the northern central Andes (see Section 2 for details).

Table 3 Detrital zircon U-Pb geochronology compilation

Data source	Sample name	Latitude	Longitude	*n*	Physiographic region	Formation or group name	Eon	Era	Period	Epoch
Sundell et al. (2018); this study[a]	20140608–03[a]	−13.76799	−71.82979	351	Altiplano	Paruro Fm.	Phanerozoic	Cenozoic	Neogene	Late Miocene
	20140528–01	−13.75312	−71.83511	258						
	20140605–01[a]	−13.75913	−71.82329	177						
Perez and Horton (2014)	TC076	−15.01787	−70.57599	84	Altiplano	Tinajani Fm.	Phanerozoic	Cenozoic	Neogene	Miocene
	240510–13	−15.00179	−70.57600	101						
	240510–10	−14.97278	−70.57021	96						
	240510–08	−14.93283	−70.57875	104						
	240510–05	−14.90085	−70.59019	107						
Alván et al. (2015)	CAM-11-22	−16.57004	−72.64555	50	C. Cordillera	Camaná Fm.	Phanerozoic	Cenozoic	Neogene	L. Oligocene-L. Miocene
	CAM-12-10	−16.57599	−72.62951	21						
	CAM-11-02	−16.57871	−72.62829	34						
	CAM-11-03	−16.57914	−72.62833	51						
	CAM-11-01	−16.59799	−72.63109	63						
	CAM-11-16	−16.57438	−72.68980	22						
	CAM-12-01	−16.56787	−72.68846	29						
	CAM-11-13	−16.56768	−72.68796	56						
	CAM-11-05	−16.56768	−72.68796	52						
	CAM-11-20	−16.65973	−72.59396	52						
	CAM-12-08b	−16.48924	−72.93351	23						
	CAM-11-08	−16.48924	−72.93351	6						
	CAM-11-07	−16.48813	−72.93475	53						
	CAM-10-03	−16.51076	−72.91999	17						
	CAM-12-04	−16.58984	−72.69617	27						
	CAM-11-06	−16.48900	−72.93362	18						
	CAM-12-06	−16.51124	−72.92121	25						
Wotzlaw et al. (2011)	AZA-04-04	−18.58583	−69.81000	27	Altiplano	Azapata Fm.	Phanerozoic	Cenozoic	Paleogene-Neogene	L. Oligocene-Miocene
	AZA-04-06	−18.58889	−69.81528	87						
	CAM-07-03	−18.58889	−69.81528	85						
Wotzlaw et al. (2011)	AZU-08	−18.13400	−68.11600	138	Altiplano	Azurita Fm.	Phanerozoic	Cenozoic	Paleogene	L. Oligocene

Sundell et al. (2018); this study[a]	20140611–03[a]	−13.62829	−71.88537	268	Altiplano	Punacancha Fm.	Phanerozoic	Cenozoic	Paleogene	Oligocene
	20140611–01[a]	−13.61641	−71.87318	385						
Perez and Horton (2014)	220510–11	−14.71732	−70.69929	110	Altiplano	Puno Gp.	Phanerozoic	Cenozoic	Paleogene	Oligocene
	220510–10	−14.71674	−70.69931	104						
	220510–08	−14.71420	−70.69843	98						
	220510–07	−14.71375	−70.69754	102						
	NPPR12–20	−14.90273	−70.52791	96						
Sundell et al. (2018); this study[a]	20150525–02[a]	−13.61761	−71.84363	422	Altiplano	San Jerónimo Gp.	Phanerozoic	Cenozoic	Paleogene	Eocene
	20150520–01[a]	−13.69650	−71.85138	380						
Sundell et al. (2018); this study[a]	20150519–03[a]	−13.69364	−71.84798	378	Altiplano	Quilque Fm.	Phanerozoic	Cenozoic	Paleogene	Paleocene
Perez et al. (2016)	13PR07	−14.40811	−70.48677	98	*E. cordillera*	Viluyo Fm.	Phanerozoic	Mesozoic	L. Cretaceous	
	13PR10	−14.42921	−70.48767	104		Auzangate Fm.				
	13PR08	−14.41558	−70.48571	104		Vilquechico Fm.				
Sundell et al. (2018)	20160813–08	−16.05183	−69.77223	316	Altiplano	Huancané Fm.	Phanerozoic	Mesozoic	E. Cretaceous	
Perez et al. (2016)	13PR06	−14.40408	−70.48380	109	E. Cordillera					
Sundell et al. (2018)	20160814–15	−16.27508	−70.19324	209	W. Cordillera	Hualhuani Fm.	Phanerozoic	Mesozoic	E. Cretaceous	
	20160815–06	−15.86207	−70.44615	121						
Perez and Horton (2014)	NPPR12–25	−14.37551	−70.54854	92	E. Cordillera	Muni Fm.	Phanerozoic	Mesozoic	E. Cretaceous	
	NPDZP003	−14.70961	−70.59646	89						
Sundell et al. (2018)	20160815–04	−15.85268	−70.30539	304	W. Cordillera	Labra Fm.	Phanerozoic	Mesozoic	L. Jurassic	
Sundell et al. (2018)	20160815–05	−15.86480	−70.42625	303	W. Cordillera	Puente Fm.	Phanerozoic	Mesozoic	L. Jurassic	
Wotzlaw et al. (2011)	LOC-08-04	−18.77900	−70.13200	87	C. Cordillera	Mesozoic substratum	Phanerozoic	Mesozoic	Jurassic-Cretaceous	
	AZA-07-01	−18.59056	−69.81417	85						
	GUA-08-02	−19.06800	−70.05300	61						
	GUA-08-04	−18.59056	−69.81417	42						

Continued

Table 3 Detrital zircon U-Pb geochronology compilation—Cont'd

Data source	Sample name	Latitude	Longitude	*n*	Physiographic region	Formation or group name	Eon	Era	Period	Epoch
Decou et al. (2013)	YUR-08-03	−16.19322	−71.82862	115	C. Cordillera	Mesozoic Basement	Phanerozoic	Mesozoic	Jurassic	
Boekhout et al. (2013)	09FB150	−15.87100	−74.24810	33	C. Cordillera	Yura Gp.	Phanerozoic	Mesozoic	L. Triassic-E. Jurassic	
	09FB124	−16.98520	−71.74820	57						
	09FB88	−17.56987	−70.03173	51						
Boekhout et al. (2013)	09FB87	−17.56990	−70.03170	61	C. Cordillera	Yamayo Gp.	Phanerozoic	Mesozoic	Triassic	
	09FB77	−17.67990	−70.08710	72						
	09FB17	−15.96660	−74.04140	83						
	09FB71	−17.60890	−70.06060	58						
Perez and Horton (2014)	NPDZP006	−13.85975	−70.51526	96	E. Cordillera	Mitu Gp.	Phanerozoic	Mesozoic	Permo-Triassic	
Boekhout et al. (2013)	09FB125	−16.31290	−72.45360	48	C. Cordillera	Yamayo Gp.	Phanerozoic	Paleozoic	Carboniferous-Permian	
	09FB120	−16.98520	−71.74820	7						
	09FB16	−15.99980	−74.02630	59						
	09FB119	−17.04660	−71.72310	18						
	09FB132	−16.40280	−73.13910	42						
	09FB30	−17.44850	−71.38100	47						
	09FB31	−17.44850	−71.38100	73						
	09FB152	−13.91870	−76.34900	72						
Perez and Horton (2014)	NPDZP004	−14.35608	−70.55628	98	E. Cordillera	Ambo Fm.	Phanerozoic	Paleozoic	E. Carboniferous	
Leier et al. (2010)	RL2	−17.07095	−67.63562	98	E. Cordillera	Devonian-Carboniferous strata	Phanerozoic	Paleozoic	L. Devonian-Carboniferous	
	RL3	−17.05260	−67.67143	97						
	RL4	−17.04988	−67.66633	104						
Leier et al. (2010)	RL1	−17.12247	−67.59867	100	E. Cordillera	Villa Villa Fm.	Phanerozoic	Paleozoic	Devonian	
Reimann et al. (2010)	La1	−15.29212	−70.33677	75	Altiplano	Lampa Fm.	Phanerozoic	Paleozoic	Devonian	

Reimann et al. (2010)	Cab6	−15.62735	−70.38471	107	Altiplano	Cabanillas Gp.	Phanerozoic	Paleozoic	Devonian	
	Cab18	−15.63089	−70.38242	88						
Reimann et al. (2010)	Co12	−17.03845	−71.71873	115	C. Cordillera	Cabanillas Gp.	Phanerozoic	Paleozoic	Devonian	
	Et2	−17.55766	−70.03174	104						
	Ba2	−16.31080	−72.45445	134						
	To5	−16.29662	−72.45085	136						
Leier et al. (2010)	RL5	−17.02345	−67.67003	98	E. Cordillera	Silurian-Devonian strata	Phanerozoic	Paleozoic	L. Silurian-E. Devonian	
	RL6	−17.01485	−67.66342	94						
	RL7	−17.00285	−67.65598	95						
Perez and Horton (2014)	TC054	−14.84825	−70.56136	103	E. Cordillera	San Gaban Fm.	Phanerozoic	Paleozoic	Ordovician	
Bahlburg et al. (2011)	Oy13	−13.21600	−72.58700	118	E. Cordillera	Ollantaytambo Fm.	Phanerozoic	Paleozoic	Ordovician	
Reimann et al. (2010)	San 12	−14.14366	−69.28065	118	E. Cordillera	Sandia Fm.	Phanerozoic	Paleozoic	Ordovician	
	San 17	−14.25353	−69.40898	111						
Reimann et al. (2010)	Coro 18	−16.26904	−67.82120	124	E. Cordillera	Amutara Fm.	Phanerozoic	Paleozoic	Ordovician	
	Am 20	−16.32674	−67.97069	127						
Reimann et al. (2010)	Ja7	−15.31527	−70.24419	120	Altiplano	Calapuja Fm.	Phanerozoic	Paleozoic	Ordovician	
Chew et al. (2008)	SJ-11	−15.40684	−75.13898	45	C. Cordillera	Chicuerìo and San Juan Fms.	Proterozoic	Neoproterozoic		
	SJ-16	−15.40685	−75.14085	69						
	SJ-57	−15.39133	−75.15592	60						
Casquet et al. (2010)	CAM-7	−16.51119	−72.63794	28	C. Cordillera	Arequipa basement	Proterozoic			
	OCO-26	−16.44236	−73.12353	105						
	QUI-16	−16.68314	−72.33497	17						

C. Cordillera, Coastal Cordillera; W. Cordillera, Western Cordillera; E. Cordillera, Eastern Cordillera.
[a]*Indicates samples with new data from this study.*

detrital age distributions show similar characteristic age populations and relative proportions of those populations when the <200 Ma ages are removed (Fig. 9D). The similar characteristic age populations and proportions of those age populations further suggest there was little addition of detrital zircons from older age provinces, as the proportions of individual age populations would be expected to change with continued input. Instead, the northern central Andes were regionally isolated from sediment input from older tectonic provinces, and existing strata were continually reworked, redistributed, and redeposited, along with new volcaniclastic material derived from pervasive magmatism throughout the Mesozoic and Cenozoic.

5.3 Crustal evolution of western South America

Combined U-Pb and εHf(t) isotopic results provide insight into the crustal evolution of major orogenic events along the western margin of South America. Detrital zircons >1300 Ma are dominated by moderately juvenile εHf(t) values (Figs. 4A and 7B), which suggests that craton formation involved some recycling of older crust. εHf(t) values decrease with decreasing age along a similar slope as the average crustal evolution trajectory (Fig. 4A), suggesting progressive incorporation of existing cratonic material and increased crustal recycling from 2500 to 1500 Ma. This trend continues in 1300–900 Ma zircons, suggesting that crustal recycling continued during Sunsás-Grenville orogenesis (Figs. 4A and 7B). Approximately half of the zircons within the 1300–900 Ma age range lie on the average crustal evolution array, which passes through the older, >1300 Ma zircons, suggesting that these zircons may have been derived from magmatic material that incorporated earlier cratonic material. However, results plotted as bivariate KDEs highlight two dominant clusters of εHf(t) values for 1300–900 Ma zircons, with roughly half that lie above the CHUR line, which cannot be back-projected along an average crustal evolution array to older εHf values (Fig. 7B). This indicates there was some generation of new crust at this time, or alternatively there was extreme mixing of juvenile and evolved crust. Detrital zircons between 800 and 500 Ma show the most dispersion and isotopic pull down to negative εHf(t) values of any age group (Figs. 4A and 5D). These zircons likely formed from a mixture of magmatic material that incorporated a significant amount of Sunsás-Grenville crust, as nearly all of the εHf(t) values can be projected back in time along the average crustal evolution trajectory to 1300–900 Ma εHf(t) values, indicating crustal recycling and incorporation of that older crustal material increased throughout the Proterozoic.

Detrital zircons from Cenozoic Altiplano strata show an increase in εHf(t) values from the Neoproterozoic to present, indicating that the overall amount of crustal recycling decreases during this time interval. Roughly half of the detrital zircons younger than 350 Ma do not appear to have incorporated any significant amount of older crustal material (barring extreme mixing of very old and very young crustal material), suggesting increased generation of new crust. However, many of the ages <350 Ma (roughly half) could have been produced by a mixture of the more juvenile portions of the Sunsás-Grenville and/or Pampean-Braziliano crust, indicating that although crustal recycling does appear to decrease since the Neoproterozoic, it was still an important process during Andean orogenesis. This indicates there was less crustal recycling and increased crustal generation through time along the west-central margin of South America since the late Paleozoic.

Detrital zircons from the Cenozoic Altiplano show similar results to previously published εHf(t) values and indirectly to εNd(t) values from in situ igneous and metamorphic rocks, as well as to detrital zircons from Paleozoic sandstones and modern rivers ($n = 660$ in situ igneous and metamorphic ages;

$n = 1770$ detrital ages) (Figs. 6 and 7). Combined U-Pb and εHf(t) results point to increasing amounts of crustal recycling throughout the Proterozoic, with peak crustal recycling in the early Paleozoic indicated by the decrease in εHf(t) and εNd(t) values during the late Neoproterozoic-early Paleozoic (Fig. 7B and C). This same trend, albeit with more dispersion, is also seen in the detrital data compilation (Fig. 7A). This supports the hypothesis of decreased crustal recycling and increased crustal generation since the Neoproterozoic.

The decrease in crustal recycling since the late Paleozoic is consistent with geodynamic models of accretionary orogenesis (e.g., Collins et al., 2011). Models of ocean-continent subduction predict progressive removal of continental lower crust and lithospheric mantle from beneath the arc and backarc through ongoing mechanical and/or thermal processes, which can take place hundreds of km inboard of the subduction trench (Hyndman et al., 2005). Convective thinning of mantle lithosphere via mantle flow appears to be a long-lived feature in most of these systems (Currie et al., 2008). Convective thinning takes place in both ocean-ocean and ocean-continent subduction systems, and irrespective of second-order dynamics of the subduction system through time such as advancing or retreating subduction of the trench (Collins et al., 2011).

The western margin of South America is considered an "external" subduction system, as typified by subduction in the circum-Pacific ring-of-fire region (Collins et al., 2011). Progressive removal of lower crust and lithospheric mantle in external subduction systems, and a shift toward more positive εHf(t) values, is a globally observed trend in accretionary orogenic systems due to magmatic underplating or tectonic accretion, regardless of retreating or advancing subduction (Collins et al., 2011). Thus, the general trend toward more juvenile εHf(t) values in the Phanerozoic central Andes is one to be expected since the establishment of this long-lived ocean-continent convergent margin.

5.4 Cyclical orogenesis

There has been considerable debate about whether or not Cordilleran orogenesis is controlled by cyclical geodynamic processes (e.g., Haschke et al., 2002, 2006; Ramos, 2009; DeCelles et al., 2009, 2015b). The general idea is that the Andes formed due to predictable, cyclical episodes of magmatism, crustal deformation, crustal thickening, and surface uplift. Much of the research in the central Andes in support of the orogenic cyclicity model has focused on northwestern Argentina (e.g., Carrapa and DeCelles, 2015; DeCelles et al., 2015b). Geodynamic processes involving both the upper and lower plates (overriding and subducting lithosphere) have been invoked as the primary drivers of orogenic cycles. Upper plate controls include lithospheric thickening through shortening (Lamb, 2011), magmatic addition (Francis and Hawkesworth, 1994), relamination (Hacker et al., 2011), crustal flow (Barke and Lamb, 2006), thinning through foundering of Rayleigh-Taylor instabilities (Krystopowicz and Currie, 2013) or delamination (Bird, 1979), and underthrusting of continental lithosphere (DeCelles et al., 2009, 2015b). Lower plate controls include slab flattening and steepening (Ramos, 2009), and repeated slab breakoff (Haschke et al., 2002). There are conflicting views as to which of these processes dominates and ultimately drives orogenic cyclicity. For example, Haschke et al. (2002, 2006) suggest cyclicity is predominantly driven by convergence rate (e.g., Somoza, 1998) and subducting slab geometry (e.g., Jordan et al., 1983), resulting in periods of high- and low-flux magmatism and slab breakoff. Ramos (2009) and Ramos et al. (2014) invoke both lower and upper plate processes, primarily slab dip for the former, and delamination of lower crust and mantle lithosphere for the latter. DeCelles et al. (2009, 2015b) invoke simple shear

underthrusting of melt-fertile continental lower crust and mantle lithosphere as the primary driver of high flux magmatism and cyclicity.

Combined U-Pb and εHf(t) data provide a test of the simple shear model for orogenic cyclicity (DeCelles et al., 2009, 2015b). If simple shear underthrusting drives cyclicity, then there should be corresponding isotopic shifts to negative εHf(t) values immediately preceding and during periods of high-flux magmatism due to the incorporation of the more evolved lithosphere of the upper plate.

Results presented here, when combined with previously published εHf(t) data, tentatively support the orogenic cyclicity model of DeCelles et al. (2015b), as U-Pb–εHf(t) patterns of detrital zircon data reveal decreasing εHf(t) trends during three age intervals: 180–140 Ma, 120–60 Ma, and 50–10 Ma (Fig. 5C). The latter two periods roughly coincide with previously reported high flux events and interpreted cyclicity from 80 to 60 Ma and 45 to 20 Ma in southern Peru based on apparent pulses of magmatism observed in compiled records of detrital and igneous crystallization ages in step with increased foreland basin sedimentation rate (Sundell et al., 2018), and a stepwise increase in Sr/Y from in situ igneous rocks (Mamani et al., 2010). Quantification of the εHf(t) time series periodicity reveals a ~72 Myr period based on frequency analysis (Fig. 10). Previous research has assigned a 25–50 Myr periodicity to the record of orogenic cyclicity (DeCelles et al., 2009), particularly to the magmatic arc of northern Chile (Haschke et al., 2002). However, other archives, including those in southern Peru (Sundell et al., 2018) and the Sierra Nevada batholith (Ducea, 2001), point to slightly longer periods. This is consistent with theoretical predictions by DeCelles et al. (2009) that the pace of isotopic pull-downs should be correlated with the rate of retroarc shortening. Although the orogenic cyclicity model remains to be further tested, our results, interpreted in the context of compiled isotopic records, provide further support that observed pulses in magmatism and apparent cyclicity in the Peruvian central Andes may be the result of cyclical orogenesis driven by simple shear underthrusting of continental lithosphere.

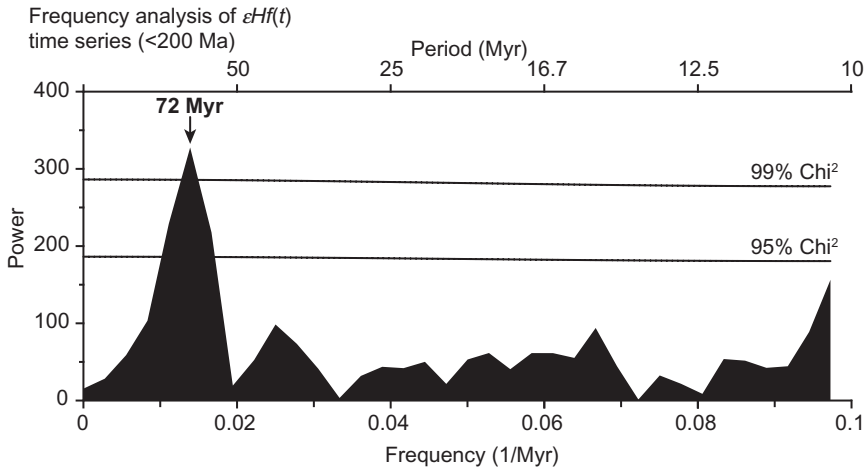

FIG. 10

Frequency analysis of the <200-Ma interval reveals a dominant 72-Myr period in the εHf(t) time series, which rises above both the 95% and 99% AR(1) red-noise false alarm chi-squared limits.

6 Conclusions

We present detrital zircon U-Pb and Hf isotopic data for sandstone samples collected from the Cenozoic Altiplano in the central Andes of southern Peru. Results suggest mixed sourcing of detrital zircons from age provinces across South America, followed by isolation and recycling of these detrital zircons since the late Paleozoic. Previously documented U-Pb and εHf(t) isotopic patterns of pre-Andean zircons from Paleozoic sandstones and modern rivers reveal similar patterns to zircons hosted in Cenozoic Altiplano sedimentary rocks and suggest they share a similar provenance. Highly evolved Late Neoproterozoic detrital zircons from Cenozoic sandstones that are absent in Ordovician-Devonian sandstones suggest initial derivation from distal regions in southeastern Brazil, potentially as part of a transcontinental drainage system that was active at some point during the Late Paleozoic to Cenozoic. Published detrital zircon data compiled for the northern central Andes show similar age distributions and proportions of individual age populations, suggesting that Paleozoic and older detrital zircons were sourced from reworked and recycled sedimentary rocks, and that this region was isolated from sediment input of Proterozoic age provinces since the late Paleozoic. Detrital zircons >1300 Ma with moderately juvenile εHf(t) values are indicative of early but limited crustal recycling, whereas εHf(t) values decrease to moderately juvenile to highly evolved from 1300 to 900 Ma and 800–500 Ma, suggesting increased incorporation of older crustal material and crustal recycling that peaks in the late Neoproterozoic. Increased εHf(t) values during Andean orogenesis indicate less crustal recycling following the establishment and transition to long-lived accretionary orogenesis in the late Paleozoic that has continued to present day. Progressive isotopic shifts to negative εHf(t) values with a periodicity of ~72 Myr provide tentative support for models of cyclical orogenesis calling on simple shear underthrusting of continental lithosphere.

Acknowledgments

We thank Erick Gil and the Gil family for logistical support in southern Peru; Richard Styron, Whitney Paola Usnayo Perales, and Dustin Villarreal for field assistance; Dan Alberts, Ryan Eden, Nicky Giesler, Kojo Plange, and Chelsi Jean White for sample preparation and laboratory assistance at the University of Arizona LaserChron Center (ALC). Juan Andrés Dahlquist, Marcia Muñoz, and Sebastián Verdecchia provided constructive reviews of this manuscript. We thank Editors Brian Horton and Andrés Folguera for the handling of this manuscript and their patience during its revision. Fieldwork was funded by the National Science Foundation (EAR-1550097). New U-Pb geochronology and Hf isotope geochemistry analytical support was provided by the ALC.

Appendix: Supplementary material

Supplementary material related to this chapter can be found on the accompanying CD or online at https://doi.org/10.1016/B978-0-12-816009-1.00014-9.

References

Aceñolaza, F.G., Toselli, A., 1984. Lower Ordovician Volcanism in North West Argentina. Aspects of the Ordovician System. vol. 295 Paleontological Contributions of the University of Oslo, pp. 203–209.

Allmendinger, R.W., Jordan, T.E., Kay, S.M., Isacks, B.L., 1997. The evolution of the Altiplano-Puna plateau of the Central Andes. Annu. Rev. Earth Planet. Sci. 25 (1), 139–174.

Alván, A., von Eynatten, H., Dunkl, I., Gerdes, A., 2015. Zircon U–Pb geochronology and heavy mineral composition of the Camaná Formation, southern Peru: constraints on sediment provenance and uplift of the Coastal and Western Cordilleras. J. S. Am. Earth Sci. 61, 14–32.

Augustsson, C., Muenker, C., Bahlburg, H., Fanning, C.M., 2006. Provenance of late Palaeozoic metasediments of the SW South American Gondwana margin: a combined U–Pb and Hf-isotope study of single detrital zircons. J. Geol. Soc. 163 (6), 983–995.

Babinski, M., Chemale Jr., F., Hartmann, L.A., Van Schmus, W.R., Carlos da Silva, L., 1996. Juvenile accretion at 750–700 Ma in southern Brazil. Geology 24 (5), 439–442.

Bahlburg, H., Vervoort, J.D., Du Frane, S.A., Bock, B., Augustsson, C., Reimann, C., 2009. Timing of crust formation and recycling in accretionary orogens: insights learned from the western margin of South America. Earth Sci. Rev. 97 (1), 215–241.

Bahlburg, H., Vervoort, J.D., DuFrane, S.A., Carlotto, V., Reimann, C., Cárdenas, J., 2011. The U–Pb and Hf isotope evidence of detrital zircons of the Ordovician Ollantaytambo Formation, southern Peru, and the Ordovician provenance and paleogeography of southern Peru and northern Bolivia. J. S. Am. Earth Sci. 32 (3), 196–209.

Barke, R., Lamb, S., 2006. Late Cenozoic uplift of the Eastern Cordillera, Bolivian Andes. Earth Planet. Sci. Lett. 249 (3), 350–367.

Belousova, E., Griffin, W.L., O'Reilly, S.Y., Fisher, N.L., 2002. Igneous zircon: trace element composition as an indicator of source rock type. Contrib. Mineral. Petrol. 143 (5), 602–622.

Belousova, E.A., Kostitsyn, Y.A., Griffin, W.L., Begg, G.C., O'Reilly, S.Y., Pearson, N.J., 2010. The growth of the continental crust: constraints from zircon Hf-isotope data. Lithos 119 (3–4), 457–466.

Bird, P., 1979. Continental delamination and the Colorado Plateau. J. Geophys. Res. 84 (B13), 7561–7571.

Blichert-Toft, J., 2001. On the Lu-Hf isotope geochemistry of silicate rocks. Geostand. Geoanal. Res. 25 (1), 41–56.

Boekhout, F., Sempéré, T., Spikings, R., Schaltegger, U., 2013. Late Paleozoic to Jurassic chronostratigraphy of coastal southern Peru: Temporal evolution of sedimentation along an active margin. J. S. Am. Earth Sci. 47, 179–200.

Boekhout, F., Roberts, N.M., Gerdes, A., Schaltegger, U., 2015. A Hf-isotope perspective on continent formation in the south Peruvian Andes. Geol. Soc. Lond., Spec. Publ. 389 (1), 305–321.

Botev, Z.I., Grotowski, J.F., Kroese, D.P., 2010. Kernel density estimation via diffusion. Ann. Stat. 38 (5), 2916–2957.

Bouvier, A., Vervoort, J.D., Patchett, P.J., 2008. The Lu–Hf and Sm–Nd isotopic composition of CHUR: constraints from unequilibrated chondrites and implications for the bulk composition of terrestrial planets. Earth Planet. Sci. Lett. 273 (1–2), 48–57.

Cardona, A., Cordani, U.G., Ruiz, J., Valencia, V.A., Armstrong, R., Chew, D., Sanchez, A.W., 2009. U-Pb zircon geochronology and Nd isotopic signatures of the pre-Mesozoic metamorphic basement of the eastern Peruvian Andes: growth and provenance of a late Neoproterozoic to carboniferous accretionary orogen on the northwest margin of Gondwana. J. Geol. 117 (3), 285–305.

Carlotto, V., 2013. Paleogeographic and tectonic controls on the evolution of Cenozoic basins in the Altiplano and Western cordillera of southern Peru. Tectonophysics 589, 195–219.

Carrapa, B., DeCelles, P.G., 2015. Regional exhumation and kinematic history of the Central Andes in response to cyclical orogenic processes. Geol. Soc. Am. Mem. 212, 201–213.

Casquet, C., Fanning, C.M., Galindo, C., Pankhurst, R.J., Rapela, C.W., Torres, P., 2010. The Arequipa massif of Peru: New SHRIMP and isotope constraints on a Paleoproterozoic inlier in the Grenvillian orogen. J. S. Am. Earth Sci. 29 (1), 128–142.

Cherniak, D.J., Hanchar, J.M., Watson, E.B., 1997. Diffusion of tetravalent cations in zircon. Contrib. Mineral. Petrol. 127 (4), 383–390.

Chew, D.M., Schaltegger, U., Košler, J., Whitehouse, M.J., Gutjahr, M., Spikings, R.A., Miškovic, A., 2007. U-Pb geochronologic evidence for the evolution of the Gondwanan margin of the north-Central Andes. Geol. Soc. Am. Bull. 119 (5–6), 697–711.

Chew, D.M., Magna, T., Kirkland, C.L., Mišković, A., Cardona, A., Spikings, R., Schaltegger, U., 2008. Detrital zircon fingerprint of the Proto-Andes: evidence for a Neoproterozoic active margin? Precambrian Res. 167 (1), 186–200.

Cobbing, E.J., Ozard, J.M., Snelling, N.J., 1977. Reconnaissance geochronology of the crystalline basement rocks of the Coastal Cordillera of southern Peru. Geol. Soc. Am. Bull. 88 (2), 241–246.
Collins, W.J., Belousova, E.A., Kemp, A.I., Murphy, J.B., 2011. Two contrasting Phanerozoic orogenic systems revealed by hafnium isotope data. Nat. Geosci. 4 (5), 333.
Cordani, U.G., Sato, K., 1999. Crustal evolution of the South American platform, based on Nd isotopic systematics on granitoid rocks. Episodes 22 (3), 167–173 (Newsmagazine of the International Union of Geological Sciences).
Cordani, U.G., Teixeira, W., D'Agrella-Filho, M.S., Trindade, R.I., 2009. The position of the Amazonian Craton in supercontinents. Gondwana Res. 15 (3–4), 396–407.
Currie, C.A., Huismans, R.S., Beaumont, C., 2008. Thinning of continental backarc lithosphere by flow-induced gravitational instability. Earth Planet. Sci. Lett. 269 (3–4), 436–447.
Dahlquist, J.A., Pankhurst, R.J., Gaschnig, R.M., Rapela, C.W., Casquet, C., Alasino, P.H., … Baldo, E.G., 2013. Hf and Nd isotopes in early Ordovician to early carboniferous granites as monitors of crustal growth in the Proto-Andean margin of Gondwana. Gondwana Res. 23 (4), 1617–1630.
Darwin, C., 1846. Geological Observations on South America: Being the Third Part of the Geology of the Voyage of the Beagle, Under the Command of Capt. Fitzroy, RN During the Years 1832 to 1836. Vol. 3 Createspace Independent Publishing Platform.
de Assis Janasi, V., 2002. Elemental and Sr–Nd isotope geochemistry of two Neoproterozoic mangerite suites in SE Brazil: implications for the origin of the mangerite–charnockite–granite series. Precambrian Res. 119 (1–4), 301–327.
De Haller, A., Corfu, F., Fontboté, L., Schaltegger, U., Barra, F., Chiaradia, M., Alvarado, J.Z., 2006. Geology, geochronology, and Hf and Pb isotope data of the Raúl-Condestable iron oxide-copper-gold deposit, central coast of Peru. Econ. Geol. 101 (2), 281–310.
DeCelles, P.G., Ducea, M.N., Kapp, P., Zandt, G., 2009. Cyclicity in Cordilleran orogenic systems. Nat. Geosci. 2 (4), 251.
DeCelles, P.G., Ducea, M.N., Carrapa, B., Kapp, P.A., 2015a. Geodynamics of a Cordilleran Orogenic System: The Central Andes of Argentina and Northern Chile. Geological Society of America.
DeCelles, P.G., Zandt, G., Beck, S., Currie, C., Ducea, M.N., Kapp, P., et al., 2015b. Cyclical orogenic processes in the Cenozoic Central Andes. Geol. Soc. Am. Mem. 212, 212–222.
Decou, A., Von Eynatten, H., Dunkl, I., Frei, D., Wörner, G., 2013. Late Eocene to Early Miocene Andean uplift inferred from detrital zircon fission track and U–Pb dating of Cenozoic forearc sediments (15–18 S). J. S. Am. Earth Sci. 45, 6–23.
Demouy, S., Paquette, J.-L., de Saint Blanquat, M., Benoit, M., Belousova, E.A., O'Reilly, S.Y., et al., 2012. Spatial and temporal evolution of Liassic to Paleocene arc activity in southern Peru unraveled by zircon U–Pb and Hf in-situ data on plutonic rocks. Lithos 155, 183–200.
DePaolo, D.J., 1988. Age dependence of the composition of continental crust: evidence from Nd isotopic variations in granitic rocks. Earth Planet. Sci. Lett. 90 (3), 263–271.
Dhuime, B., Hawkesworth, C., Cawood, P., 2011. When continents formed. Science 331 (6014), 154–155.
Ducea, M., 2001. The California arc: thick granitic batholiths, eclogitic residues, lithospheric-scale thrusting, and magmatic flare-ups. GSA Today 11, 4–10.
Forbes, D., 1861. On the geology of Bolivia and southern Peru. Q. J. Geol. Soc. 17 (1–2), 7–62.
Francis, P.W., Hawkesworth, C.J., 1994. Late Cenozoic rates of magmatic activity in the Central Andes and their relationships to continental crust formation and thickening. J. Geol. Soc. 151 (5), 845–854.
Fuck, R.A., Jardim de Sá, E.F., Pimentel, M.M., Dardenne, M.A., Pedrosa-Soares, A.C., 1993. As faixas de dobramentos marginais do Cráton do São Francisco: síntese dos conhecimentos. O Cráton do São Francisco, pp. 161–185.
Gehrels, G., 2014. Detrital zircon U-Pb geochronology applied to tectonics. Annu. Rev. Earth Planet. Sci. 42, 127–149.

Gehrels, G., Pecha, M., 2014. Detrital zircon U-Pb geochronology and Hf isotope geochemistry of Paleozoic and Triassic passive margin strata of western North America. Geosphere 10 (1), 49–65.

Gehrels, G.E., Valencia, V.A., Ruiz, J., 2008. Enhanced precision, accuracy, efficiency, and spatial resolution of U-Pb ages by laser ablation–multicollector–inductively coupled plasma–mass spectrometry. Geochem. Geophys. Geosyst. 9 (3).

Gehrels, G.E., Blakey, R., Karlstrom, K.E., Timmons, J.M., Dickinson, B., Pecha, M., 2011. Detrital zircon U-Pb geochronology of Paleozoic strata in the Grand Canyon, Arizona. Lithosphere 3 (3), 183–200.

Griffin, W.L., Belousova, E.A., Shee, S.R., Pearson, N.J., O'reilly, S.Y., 2004. Archean crustal evolution in the northern Yilgarn Craton: U–Pb and Hf-isotope evidence from detrital zircons. Precambrian Res. 131 (3–4), 231–282.

Hacker, B.R., Kelemen, P.B., Behn, M.D., 2011. Differentiation of the continental crust by relamination. Earth Planet. Sci. Lett. 307 (3–4), 501–516.

Hammer, Ø., Harper, D.A.T., Ryan, P.D., 2001. PAST: paleontological statistics software package for education and data analysis. Palaeontol. Electron. 4, 9.

Hartz, E.H., Torsvik, T.H., 2002. Baltica upside down: a new plate tectonic model for Rodinia and the Iapetus Ocean. Geology 30 (3), 255–258.

Haschke, M.R., Scheuber, E., Günther, A., Reutter, K.J., 2002. Evolutionary cycles during the Andean orogeny: repeated slab breakoff and flat subduction? Terra Nova 14 (1), 49–55.

Haschke, M., Günther, A., Melnick, D., Echtler, H., Reutter, K.J., Scheuber, E., Oncken, O., 2006. Central and Southern Andean tectonic evolution inferred from arc magmatism. In: The Andes. Springer, Berlin, Heidelberg, pp. 337–353.

Hawkesworth, C.J., Dhuime, B., Pietranik, A.B., Cawood, P.A., Kemp, A.I.S., Storey, C.D., 2010. The generation and evolution of the continental crust. J. Geol. Soc. 167 (2), 229–248.

Horton, B.K., Perez, N.D., Fitch, J.D., Saylor, J.E., 2015. Punctuated shortening and subsidence in the Altiplano Plateau of southern Peru: implications for early Andean mountain building. Lithosphere 7 (2), 117–137.

Hyndman, R.D., Currie, C.A., Mazzotti, S.P., 2005. Subduction zone backarcs, mobile belts, and orogenic heat. GSA Today 15 (2), 4–10.

Ibanez-Mejia, M., Gehrels, G.E., Ruiz, J., Vervoort, J.D., Eddy, M.P., Li, C., 2014. Small-volume baddeleyite (ZrO2) U–Pb geochronology and Lu–Hf isotope geochemistry by LA-ICP-MS. Techniques and applications. Chem. Geol. 384, 149–167.

Isacks, B.L., 1988. Uplift of the central Andean plateau and bending of the Bolivian orocline. J. Geophys. Res. 93 (B4), 3211–3231.

Jordan, T.E., Isacks, B.L., Allmendinger, R.W., Brewer, J.A., Ramos, V.A., Ando, C.J., 1983. Andean tectonics related to geometry of subducted Nazca plate. Geol. Soc. Am. Bull. 94 (3), 341–361.

Kontak, D.J., Clark, A.H., Farrar, E., Archibald, D.A., Baadsgaard, H., 1990. Late Paleozoic-early Mesozoic magmatism in the Cordillera de Carabaya, Puno, southeastern Peru: Geochronology and petrochemistry. J. S. Am. Earth Sci. 3 (4), 213–230.

Košler, J., Fonneland, H., Sylvester, P., Tubrett, M., Pedersen, R.B., 2002. U–Pb dating of detrital zircons for sediment provenance studies—a comparison of laser ablation ICPMS and SIMS techniques. Chem. Geol. 182 (2–4), 605–618.

Krystopowicz, N.J., Currie, C.A., 2013. Crustal eclogitization and lithosphere delamination in orogens. Earth Planet. Sci. Lett. 361, 195–207.

Lamb, S., 2011. Did shortening in thick crust cause rapid late Cenozoic uplift in the northern Bolivian Andes? J. Geol. Soc. 168 (5), 1079–1092.

Leier, A.L., McQuarrie, N., Horton, B.K., Gehrels, G.E., 2010. Upper Oligocene conglomerates of the Altiplano, central Andes: the record of deposition and deformation along the margin of a hinterland basin. J. Sediment. Res. 80 (8), 750–762.

Loewy, S.L., Connelly, J.N., Dalziel, I.W., 2004. An orphaned basement block: the Arequipa-Antofalla basement of the central Andean margin of South America. Geol. Soc. Am. Bull. 116 (1–2), 171–187.

Mamani, M., Wörner, G., Sempere, T., 2010. Geochemical variations in igneous rocks of the central Andean orocline (13 S to 18 S): Tracing crustal thickening and magma generation through time and space. Geol. Soc. Am. Bull. 122 (1–2), 162–182.

Martins, V.T.D.S., Teixeira, W., Noce, C.M., Pedrosa-Soares, A.C., 2004. Sr and Nd characteristics of Brasiliano/Pan-African granitoid plutons of the Araçuaí Orogen, Southeastern Brazil: tectonic implications. Gondwana Res. 7 (1), 75–89.

Miller, J.F., Harris, N.B.W., 1989. Evolution of continental crust in the Central Andes; constraints from Nd isotope systematics. Geology 17 (7), 615–617.

Mišković, A., Schaltegger, U., 2009. Crustal growth along a non-collisional cratonic margin: a Lu–Hf isotopic survey of the Eastern Cordilleran granitoids of Peru. Earth Planet. Sci. Lett. 279 (3–4), 303–315.

Montecinos, P., Schärer, U., Vergara, M., Aguirre, L., 2008. Lithospheric origin of Oligocene–Miocene magmatism in Central Chile: U–Pb ages and Sr–Pb–Hf isotope composition of minerals. J. Petrol. 49 (3), 555–580.

Moon, H.P., 1939. III. The geology and physiography of the Altiplano of Peru and Bolivia. Trans. Linn. Soc. Lond. 1 (1), 27–43.

Newell, N.D., 1949. Geology of the Lake Titicaca region, Peru and Bolivia. Geol. Soc. Am. Mem. 36, 1–124.

Otamendi, J.E., Ducea, M.N., Cristofolini, E.A., Tibaldi, A.M., Camilletti, G.C., Bergantz, G.W., 2017. U-Pb ages and Hf isotope compositions of zircons in plutonic rocks from the central Famatinian arc, Argentina. J. S. Am. Earth Sci. 76, 412–426.

Pankhurst, R.J., Rapela, C.W., Saavedra, J., Baldo, E., Dahlquist, J., Pascua, I., Fanning, C.M., 1998. The Famatinian magmatic arc in the central Sierras Pampeanas: an Early to Mid-Ordovician continental arc on the Gondwana margin. Geol. Soc. London. 142 (1), 343–367. (Special Publications).

Paquette, J.L., Barbosa, J.S.F., Rohais, S., Cruz, S.C.P., Goncalves, P., Peucat, J.J., Martin, H., 2015. The geological roots of South America: 4.1 Ga and 3.7 Ga zircon crystals discovered in NE Brazil and NW Argentina. Precambrian Res. 271, 49–55.

Pepper, M., Gehrels, G., Pullen, A., Ibanez-Mejia, M., Ward, K.M., Kapp, P., 2016. Magmatic history and crustal genesis of western South America: Constraints from U-Pb ages and Hf isotopes of detrital zircons in modern rivers. Geosphere 12 (5), 1532–1555.

Perez, N.D., Horton, B.K., 2014. Oligocene-Miocene deformational and depositional history of the Andean hinterland basin in the northern Altiplano plateau, southern Peru. Tectonics 33 (9), 1819–1847.

Perez, N.D., Horton, B.K., McQuarrie, N., Stuebner, K., Ehlers, T.A., 2016. Andean shortening, inversion and exhumation associated with thin-and thick-skinned deformation in southern Peru. Geol. Mag. 153 (5–6), 1013–1041.

Pimentel, M.M., Fuck, R.A., 1992. Neoproterozoic crustal accretion in central Brazil. Geology 20 (4), 375–379.

Polliand, M., Schaltegger, U., Frank, M., Fontbote, L., 2005. Formation of intra-arc volcanosedimentary basins in the western flank of the central Peruvian Andes during Late Cretaceous oblique subduction: field evidence and constraints from U–Pb ages and Hf isotopes. Int. J. Earth Sci. 94 (2), 231–242.

Rak, A.J., McQuarrie, N., Ehlers, T.A., 2017. Kinematics, exhumation, and sedimentation of the north Central Andes (Bolivia): an integrated thermochronometer and thermokinematic modeling approach. Tectonics 36 (11), 2524–2554.

Ramos, V., 1999. Plate tectonic setting of the Andean Cordillera. Episodes 22, 183–190.

Ramos, V.A., 2009. Anatomy and global context of the Andes: main geologic features and the Andean orogenic cycle. Geol. Soc. Am. Mem. 204, 31–65.

Ramos, V.A., Litvak, V.D., Folguera, A., Spagnuolo, M., 2014. An Andean tectonic cycle: from crustal thickening to extension in a thin crust (34–37 SL). Geosci. Front. 5 (3), 351–367.

Rapela, C.W., Pankhurst, R.J., Casquet, C., Baldo, E., Saavedra, J., Galindo, C., 1998. Early evolution of the proto-Andean margin of South America. Geology 26 (8), 707–710.

Rapela, C.W., Pankhurst, R.J., Fanning, C.M., Grecco, L.E., 2003. Basement evolution of the Sierra de la Ventana Fold Belt: new evidence for Cambrian continental rifting along the southern margin of Gondwana. J. Geol. Soc. 160 (4), 613–628.

Reimann, C., Bahlburg, H., Kooijman, E., Berndt, J., Gerdes, A., Carlotto, V., López, S., 2010. Geodynamic evolution of the early Paleozoic Western Gondwana margin 14–17 S reflected by the detritus of the Devonian and Ordovician basins of southern Peru and northern Bolivia. Gondwana Res. 18 (2), 370–384.

Salda, L.D., Cingolani, C., Varela, R., 1992. Early Paleozoic orogenic belt of the Andes in southwestern South America: result of Laurentia-Gondwana collision? Geology 20 (7), 617–620.

Santos, J.O.S., Rizzotto, G.J., Potter, P.E., McNaughton, N.J., Matos, R.S., Hartmann, L.A., Quadros, M.E.S., 2008. Age and autochthonous evolution of the Sunsás Orogen in West Amazon Craton based on mapping and U–Pb geochronology. Precambrian Res. 165 (3–4), 120–152.

Sato, K., Siga Jr., O., Nutman, A.P., Basei, M.A., McReath, I., Kaulfuss, G., 2003. The Atuba complex, southern South American platform: Archean components and paleoproterozoic to neoproterozoic tectonothermal events. Gondwana Res. 6 (2), 251–263.

Schulz, M., Mudelsee, M., 2002. REDFIT: estimating red-noise spectra directly from unevenly spaced paleoclimatic time series. Comput. Geosci. 28, 421–426.

Scotese, C.R., 2004. A continental drift flipbook. J. Geol. 112 (6), 729–741.

Silverman, B.W., 1986. The kernel method for multivariate data. In: Density Estimation for Statistics and Data Analysis. Springer US, pp. 75–94.

Somoza, R., 1998. Updated azca (Farallon)—South America relative motions during the last 40 My: implications for mountain building in the central Andean region. J. S. Am. Earth Sci. 11 (3), 211–215.

Speer, J.A., 1980. Zircon. Rev. Mineral. Geochem. 5 (1), 67–112.

Spikings, R., Reitsma, M.J., Boekhout, F., Mišković, A., Ulianov, A., Chiaradia, M., Schaltegger, U., 2016. Characterisation of Triassic rifting in Peru and implications for the early disassembly of western Pangaea. Gondwana Res. 35, 124–143.

Stacey, J.t., Kramers, J., 1975. Approximation of terrestrial lead isotope evolution by a two-stage model. Earth Planet. Sci. Lett. 26 (2), 207–221.

Sundell, K.E., Saylor, J.E., Lapen, T.J., Styron, R.H., Villarreal, D.P., Usnayo, P., Cárdenas, J., 2018. Peruvian Altiplano stratigraphy highlights along-strike variability in foreland basin evolution of the Cenozoic Central Andes. Tectonics 37, 1876–1904. https://doi.org/10.1029/2017TC004775.

Vaughan, A.P., Pankhurst, R.J., 2008. Tectonic overview of the West Gondwana margin. Gondwana Res. 13 (2), 150–162.

Vervoort, J.D., Blichert-Toft, J., 1999. Evolution of the depleted mantle: Hf isotope evidence from juvenile rocks through time. Geochim. Cosmochim. Acta 63 (3–4), 533–556.

Vervoort, J.D., Patchett, P.J., 1996. Behavior of hafnium and neodymium isotopes in the crust: Constraints from Precambrian crustally derived granites. Geochim. Cosmochim. Acta 60 (19), 3717–3733.

Vervoort, J.D., Patchett, P.J., Blichert-Toft, J., Albarède, F., 1999. Relationships between Lu–Hf and Sm–Nd isotopic systems in the global sedimentary system. Earth Planet. Sci. Lett. 168 (1), 79–99.

Willner, A.P., Gerdes, A., Massonne, H.J., 2008. History of crustal growth and recycling at the Pacific convergent margin of South America at latitudes 29–36 S revealed by a U–Pb and Lu–Hf isotope study of detrital zircon from late Paleozoic accretionary systems. Chem. Geol. 253 (3–4), 114–129.

Wotzlaw, J.F., Decou, A., von Eynatten, H., Wörner, G., Frei, D., 2011. Jurassic to Palaeogene tectono-magmatic evolution of northern Chile and adjacent Bolivia from detrital zircon U-Pb geochronology and heavy mineral provenance. Terra Nova 23 (6), 399–406.

Further reading

Casquet, C., Rapela, C.W., Pankhurst, R.J., Baldo, E.G., Galindo, C., Fanning, C.M., Saavedra, J., 2012. A history of Proterozoic terranes in southern South America: From Rodinia to Gondwana. Geosci. Front. 3 (2), 137–145.

Fisher, C.M., Vervoort, J.D., DuFrane, S.A., 2014. Accurate Hf isotope determinations of complex zircons using the "laser ablation split stream" method. Geochem. Geophys. Geosyst. 15 (1), 121–139.

Link, P.K., Fanning, C.M., Beranek, L.P., 2005. Reliability and longitudinal change of detrital-zircon age spectra in the Snake River system, Idaho and Wyoming: An example of reproducing the bumpy barcode. Sediment. Geol. 182 (1–4), 101–142.

Patchett, P.J., Tatsumoto, M., 1980. Lu–Hf total-rock isochron for the eucrite meteorites. Nature 288 (5791), 571.

Reitsma, M., Spikings, R., Ulianov, A., Chelle-Michou, C., Gerdes, A., Chiaradia, M., Schaltegger, U., 2012. Crustal reworking in Paleozoic–Early Mesozoic orphaned back-arcs on the western Gondwana margin, south-east Peru. Reconstructing the Late Paleozoic: Early Mesozoic plutonic and sedimentary record of south-east Peru: orphaned back-arcs along the western margin of Gondwana. Vol. 9. (Doctoral dissertation).

Santos, J.O.S., Hartmann, L.A., Gaudette, H.E., Groves, D.I., Mcnaughton, N.J., Fletcher, I.R., 2000. A new understanding of the provinces of the Amazon Craton based on integration of field mapping and U-Pb and Sm-Nd geochronology. Gondwana Res. 3 (4), 453–488.

Sundell, K.E., 2017. Cenozoic surface uplift and Basin Formation in the Peruvian Central Andes. (Doctoral dissertation).

Vervoort, J.D., Patchett, P.J., Söderlund, U., Baker, M., 2004. Isotopic composition of Yb and the determination of Lu concentrations and Lu/Hf ratios by isotope dilution using MC-ICPMS. Geochem. Geophys. Geosyst. 5 (11).